Multi-layered atomic relaxation in van der Waals heterostructures

Dorri Halbertal,[1,*] Lennart Klebl,[2,*] Valerie Hsieh,[1] Jacob Cook,[3] Stephen Carr,[4] Guang Bian,[3] Cory Dean,[1] Dante M. Kennes,[2,5] and D. N. Basov[1]

[1] *Department of Physics, Columbia University, New York, New York 10027, United States*
[2] *Institut für Theorie der Statistischen Physik, RWTH Aachen University and JARA-Fundamentals of Future Information Technology, 52056 Aachen, Germany*
[3] *Department of Physics and Astronomy, University of Missouri, Columbia, MO 65211*
[4] *Physics Department, Brown University, Providence, Rhode Island 02912, United States*
[5] *Max Planck Institute for the Structure and Dynamics of Matter, Center for Free Electron Laser Science, 22761 Hamburg, Germany*

(Dated: June 15, 2022)

When two-dimensional van der Waals materials are stacked to build heterostructures, moiré patterns emerge from twisted interfaces or from mismatch in lattice constant of individual layers. Relaxation of the atomic positions is a direct, generic consequence of the moiré pattern, with many implications for the physical properties. Moiré driven atomic relaxation may be naively thought to be restricted to the interfacial layers and thus irrelevant for multi-layered heterostructures. However, we provide experimental evidence for the importance of the three dimensional nature of the relaxation in two types of van der Waals heterostructures: First, in multi-layer graphene twisted on graphite at small twist angles ($\theta \approx 0.14°$) we observe propagation of relaxation domains even beyond 18 graphene layers. Second, we show how for multi-layer $PdTe_2$ on Bi_2Se_3 the moiré lattice constant depends on the number of $PdTe_2$ layers. Motivated by the experimental findings, we developed a continuum approach to model multi-layered relaxation processes based on the generalized stacking fault energy functional given by *ab-initio* simulations. Leveraging the continuum property of the approach enables us to access large scale regimes and achieve agreement with our experimental data for both systems. Furthermore it is well known that the electronic structure of graphene sensitively depends on local lattice deformations. Therefore we study the impact of multi-layered relaxation on the local density of states of the twisted graphitic system. We identify measurable implications for the system, experimentally accessible by scanning tunneling microscopy. Our multi-layered relaxation approach is not restricted to the discussed systems, and can be used to uncover the impact of an interfacial defect on various layered systems of interest.

I. INTRODUCTION

Moiré van der Waals (vdW) heterostructures have drawn considerable interest in the past few years. Whenever two layers with relative twist or lattice mismatch are stacked, large-scale periodic perturbations of stacking configurations emerge. So called moiré superlattices hence universally appear in any kind of vdW heterostructure, including manually assembled as well as chemical vapour deposition grown [2–5] stacks. In twisted moiré heterostructures, various (unconventional) superconducting and correlated [6–34], excitonic [35–39], and topological [40–54] phases have been discovered – demonstrating that engineering heterostructures of atomically thin layers of vdW materials opens up a vast space to design properties of quantum materials [55]. However, the atomic layers in vdW materials are not rigid in general, but instead behave as deformable membranes. When two layers with an interfacial defect (i.e. lattice mismatch or twist angle) come in contact, the atomic positions relax to minimize the total energy [56].

Naturally, the relaxation itself is strongest at the defect interface, but we demonstrate here that it may also extent beyond the two atomic layers at the interface. Therefore, the "Lego bricks" analogy put forward by Geim and Grigorieva [1], where heterostructures are composed of mechanically independent layers, though extremely helpful for illustration purposes, needs to be refined considerably to incorporate the flexible nature of each layer as well as the interplay of mechanical relaxation between different layers. We contrast the two paradigms in Fig. 1, where the left panel illustrates how to understand a stack of two multi-layered, mismatched materials in the picture disregarding relaxation. As no relaxation occurs there is a sharp transition from the bottom stack (green) to the top stack (purple) visualized by the difference in width. In contrast, a multi-layered relaxation leads to a smooth deformation of layers from the bottom to the top (right panel), with signatures of the moiré superlattice slowly decaying away from the interface (yellow vortices).

In fact, we show, elaborate domain formation even far away from the interface, stressing the problem is truly three dimensional in nature. From this follows that material properties and the electronic structure [57–60] may be substantially influenced as soon as domain formation occurs, not only in direct vicinity of the interface. Figure 2 summarizes experimental evidence for the fact that the domain formation picture is rather complex, and for its three dimensional nature. Figure 2**(a-c)** explore

* These authors contributed equally

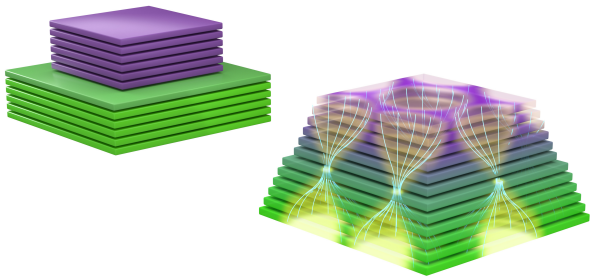

FIG. 1. Two-dimensional heterostructure composed of two mismatched (green and purple) materials. Left panel: Lego-brick-like cartoon picture in which no atomic relaxation occurs [1]. The two materials have different lattice constants visualized by the width of the stacks. Right panel: Cartoon picture including the main finding of this work: layers relax continuously away from the interface. The extent of relaxation is qualitatively encoded in the yellow color. The emergent moiré pattern slowly decays towards the outer layers of the stack.

piezoresponse force microscopy (PFM) maps of a terraced few layer graphene (FLG) structure on top of a trilayer graphene (TLG) substrate at a twist angle of 0.66° between the TLG and the FLG part of the stack. The terraced FLG has monolayer graphene (MLG), bilayer graphene (BLG), and TLG segments, shown in Fig. 2**(a-c)** respectively. As the top layer thickness increases the PFM contrast quickly decays. On the other hand, when a similar measurement is performed for a smaller twist angle of 0.14° (Fig. 2**(d-f)**) the moiré pattern can be visualized by PFM at the surface of a considerably higher stack, even up to 18 atomic layers above the twist interface (Fig. 2**(f)**). A different consequence of the layered atomic relaxation emerges in atomically mismatched heterostructures. Such a case is presented in Fig. 2**(g,h)** for an epitaxially grown $PdTe_2$ over a Bi_2Si_3 substrate. In this system a moiré superlattice emerges from the lattice mismatch between the two materials. Surprisingly, the domain shapes and even the moiré period itself seem to depend on the layer thickness of the $PdTe_2$ stack. In fact, the observed moiré period exceeds the maximal (zero twist angle) predicted moiré period, solely considering the lattice mismatch. All of the above suggest that the relaxation process and the resulting domain structures are more involved than considered thus far. The spatial extent of the relaxation process and even the moiré period depend on the twist angle and material properties.

In this work we first develop the multi-layered relaxation framework in Section II. The framework allows a description of large systems (both in terms of thickness as well as moiré period) which cannot be accessed by atomistic models [61–66]. We will then use this framework to reproduce the data in Fig. 2 (cf. Section III), explore the three dimensional nature of the relaxation process (cf. Section IV), and study its consequences for the electronic structure using graphitic stacks as a prototypical example in Section V.

II. MULTI-LAYERED RELAXATION - THE APPROACH

In this section we develop the mathematical framework to allow the description of the atomic relaxation in a multi-layered stack of vdW materials. We follow a continuous relaxation approach, conceptually similar to Refs. 67–70. By continuous relaxation, we assume that the in-plane displacement fields change on a length scale larger than the atomic unit cell spacing. Using the above assumption for continuous models, the atomic relaxation can be formulated in terms of the energy functional being a sum of a stacking mismatch and an elastic energy term. The sought after solution is the displacement field that minimizes the total energy. Ref. 67 formulated the problem in configuration space for twisted bilayer systems. Ref. 69 introduced a generalized formalism to potentially treat multiple twisted interfaces, later implemented by Ref. 68 for a specific system of double twisted trilayer graphene. In Ref. 70 we solved the problem in real space, thus allowing an omission of the periodicity requirement imposed by the previous treatments in configuration space. It allowed treating experimentally realistic strain induced relaxation patterns. The derivation follows the lines and notation of Ref. 70, but instead of treating each flake of the heterostructure as a single elastic membrane, here we assume two layered materials labelled by $j \in \{1, 2\}$ with a thickness of n_j layers, respectively, where $j = 1$ denotes the lower and $j = 2$ the upper flake of the heterostructure. Generalizations to stacks consisting of more than two flakes are conceptually straightforward. Crucially, we allow for individual relaxation in each layer with the in-plane displacement fields of layer k of flake j being described by

$$\boldsymbol{u}^{(j,k)}(\boldsymbol{r}) = \left(u_x^{(j,k)}(x,y), u_y^{(j,k)}(x,y)\right)^{\mathrm{T}} . \tag{1}$$

The interface between the two flakes is formed between layer $k = n_1$ of flake $j = 1$ and layer $k = 1$ of flake $j = 2$. The energy functional in our model is composed of the elastic energy density and the stacking energy density,

$$\mathcal{E}(\boldsymbol{r}, \boldsymbol{u}, \nabla\boldsymbol{u}) = \mathcal{E}_{\text{elastic}}(\nabla\boldsymbol{u}) + \mathcal{E}_{\text{stacking}}(\boldsymbol{r}, \boldsymbol{u}) . \tag{2}$$

We assume that the $n_1 + n_2$ displacement fields change on a length scale larger than the lattice constants α_j in accordance with prior literature [67, 69, 70]. However, Ref. 70 was restricted to a single interlayer interface, where now we consider one interface from the twist or lattice constant mismatch between flake 1 and flake 2 which after relaxation induces $n_1 - 1$ interfaces within flake 1 and similarly $n_2 - 1$ interfaces within flake 2. We show here that only such a modelling captures the important, finite penetration depth of the relaxation induced

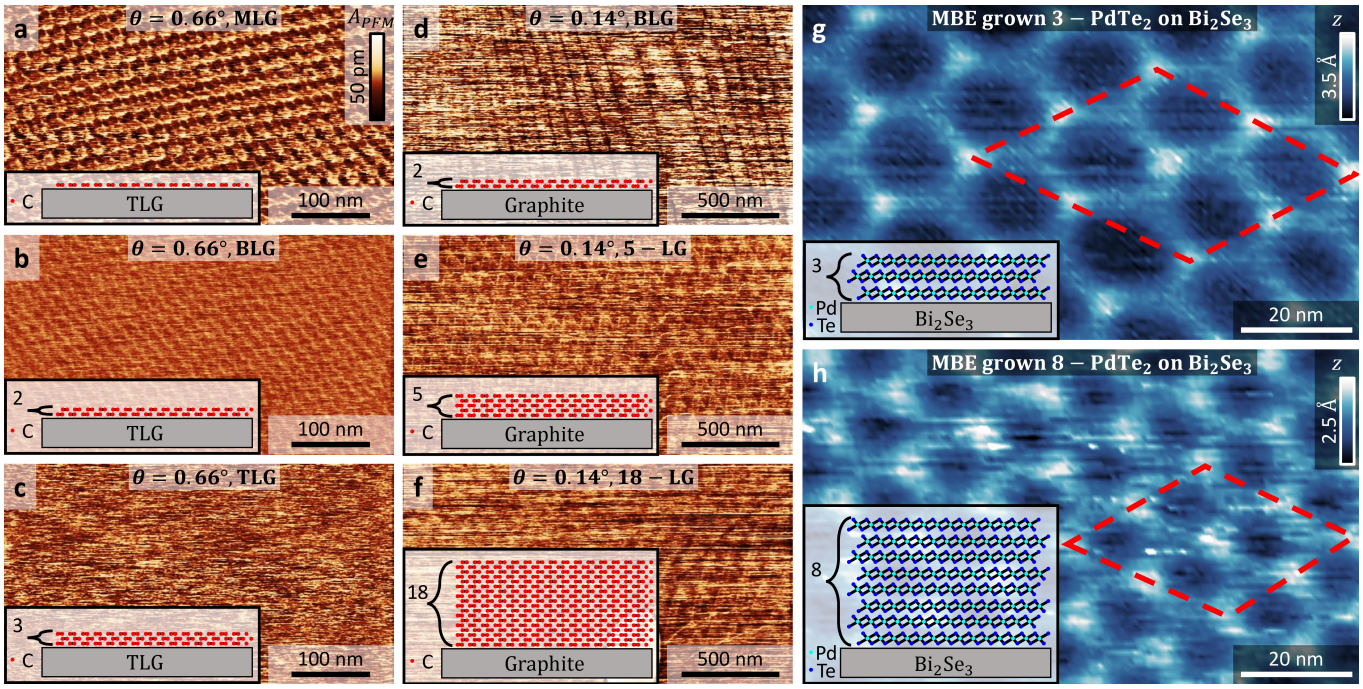

FIG. 2. **Experimental motivation: Evidence for multi-layered relaxation.** **(a-c)** Piezoelectric force microscopy (PFM) amplitude mapping of **(a)** monolayer (MLG), **(b)** bilayer (BLG) and **(c)** trilayer (TLG) graphene twisted by 0.65° relative to a TLG substrate. **(d-f)** PFM amplitude mapping of **(d)** bilayer, **(e)** 5-layered and **(f)** 18-layered graphene twisted by 0.14° relative to a graphite substrate. The smaller the twist angle the thicker the layer through which the moiré superlattice can be resolved. **(g-h)** Topography maps by scanning tunneling microscopy (STM) of molecular beam epitaxy (MBE) grown $PdTe_2$ on a Bi_2Se_3 substrate. Two thicknesses are presented 3-layers **(g)** and 8-layers **(h)**, showing a thickness dependence of the domain structure and the moiré period indicating a layer dependent relaxation process. The dashed red diamond marks four moiré unit cells (2×2) in each case. Inset in each panel presents a schematic of the system under study. The experimental details are presented in Appendices A and B

by stacking vdW heterostructures from one to a few to a large number of layers in the flakes. To this end, we will therefore assume that the stacking energy term can be described by three types of GSFEs: one covering the initial interface *between* the two flakes and two more describing the relaxation-induced interfaces *within* the two separate flakes. Note that the separation of the system into a sum over the different interfaces makes a further approximation. It neglects contributions to the stacking energy from neighboring layers beyond the nearest neighbor. Such an approximation would fail to capture subtle differences like the energy imbalance between the Bernal and rhombohedral phases in twisted double bilayer graphene [70] and could be relaxed in principle in the future.

First, we write the elastic energy density $\mathcal{E}_{\text{elastic}}(\nabla \boldsymbol{u})$ as a function of the gradients of the displacement fields $\nabla \boldsymbol{u}$:

$$\mathcal{E}_{\text{elastic}}(\nabla \boldsymbol{u}) = \sum_{j,1\leq k\leq n_j} \varepsilon^{(j,k)}(\nabla \boldsymbol{u}) = \sum_{j,1\leq k\leq n_j} \left[\frac{K_j \left(\nabla \cdot \boldsymbol{u}^{(j,k)}\right)^2}{2} + \frac{G_j}{2} \left(\left(\partial_x u_x^{(j,k)} - \partial_y u_y^{(j,k)}\right)^2 + \left(\partial_x u_y^{(j,k)} + \partial_y u_x^{(j,k)}\right)^2 \right) \right], \quad (3)$$

with $\varepsilon^{(j,k)}(\nabla \boldsymbol{u})$ the layer resolved elastic energy density, and K_j and G_j the bulk and shear moduli of flake j, respectively.

The stacking energy density, $\mathcal{E}_{\text{stacking}}(\boldsymbol{r}, \boldsymbol{u})$, explicitly depends on position and displacement fields. The general expression is a function of the stacking configuration of each interface. As the stacking configuration is defined in terms of the underlying Bravais lattice, we denote the lattice vectors of flake 1 with $\alpha_1 \boldsymbol{a}_{1,2}$ and those of flake 2 with $\alpha_2 \tilde{\boldsymbol{a}}_{1,2}$ where $\boldsymbol{a}_{1,2}$ and $\tilde{\boldsymbol{a}}_{1,2}$ are normalized lattice vectors. Here, we choose the normalization factors α_j to be the lattice constants. For the general case, the relative length of lattice vectors can be included in $\boldsymbol{a}_{1,2}$ and $\tilde{\boldsymbol{a}}_{1,2}$, and α_j acts as an overall length scale of flake j.

Further, we can always define a two-dimensional matrix $A_{1\to2}$ that transforms the lattice vectors such that

$$\begin{bmatrix}\tilde{\boldsymbol{a}}_1 & \tilde{\boldsymbol{a}}_2\end{bmatrix} = A_{1\to2}\begin{bmatrix}\boldsymbol{a}_1 & \boldsymbol{a}_2\end{bmatrix}. \tag{4}$$

We then proceed to define the stacking configuration $\boldsymbol{\Omega}_0$ of each layer in flakes 1 and 2 as

$$\boldsymbol{\Omega}_0^{(1,k)}(\boldsymbol{r},\boldsymbol{u}) = \frac{2\pi}{\alpha_1}(A_1)^{-1}\big(\boldsymbol{r}-\boldsymbol{u}^{(1,k)}(\boldsymbol{r})\big), \tag{5}$$

$$\boldsymbol{\Omega}_0^{(2,k)}(\boldsymbol{r},\boldsymbol{u}) = \frac{2\pi}{\alpha_2}(A_1)^{-1}(A_{1\to2})^{-1}\big(\boldsymbol{r}-\boldsymbol{u}^{(2,k)}(\boldsymbol{r})\big), \tag{6}$$

where we introduced the matrix notation of the lattice of the lower flake, $A_1 = \begin{bmatrix}\boldsymbol{a}_1 & \boldsymbol{a}_2\end{bmatrix}$. The origins of the unit cells of the layers within the two rigid flakes, respectively, can be chosen at $\boldsymbol{r}_1 = \alpha_1(l\boldsymbol{a}_1 + m\boldsymbol{a}_2)$ and $\boldsymbol{r}_2 = \alpha_2(l\tilde{\boldsymbol{a}}_1 + m\tilde{\boldsymbol{a}}_2)$ with integers l and m, such that for zero displacement field $\boldsymbol{\Omega}_0^{(j,k)}(\boldsymbol{r}_j,\boldsymbol{u}=0) = 2\pi(l\,,\,m)^{\mathrm{T}}$.

We assume that each unit area on each interface between two layers contributes to the stacking energy density according to the GSFE for that interface with the relative stacking configuration as input. So we define the relative stacking configuration $\boldsymbol{\Omega}_*$ for the intra-flake interfaces $k_j = 1,\dots,n_j-1$ as

$$\boldsymbol{\Omega}_*^{(1,k_1)} = -\frac{2\pi}{\alpha_2}(1+\delta)\,(A_1)^{-1}\big(\boldsymbol{u}^{(1,k_1+1)} - \boldsymbol{u}^{(1,k_1)}\big), \tag{7}$$

$$\boldsymbol{\Omega}_*^{(2,k_2)} = -\frac{2\pi}{\alpha_2}(A_1)^{-1}(A_{1\to2})^{-1}\big(\boldsymbol{u}^{(2,k_2+1)} - \boldsymbol{u}^{(2,k_2)}\big), \tag{8}$$

where we introduced the mismatch parameter $\delta = \alpha_2/\alpha_1 - 1$. The relative stacking configuration at the inter-flake interface can similarly be expressed as

$$\boldsymbol{\Omega}_*^{(1\to2)} = \frac{2\pi}{\alpha_2}(A_1)^{-1}\Big(\big((A_{1\to2})^{-1} - (1+\delta)\mathbb{1}\big)\boldsymbol{r} - (A_{1\to2})^{-1}\boldsymbol{u}^{(2,1)} + (1+\delta)\boldsymbol{u}^{(1,n_1)}\Big), \tag{9}$$

where $\mathbb{1}$ is the unity matrix in two dimensions. As we also want to explicitly treat isotropic expansion of each flake and constant stacking registry shifts of each layer (such as Bernal (AB) stacking in graphene), we define the total displacement of flake j and layer k as $\boldsymbol{U}^{(j,k)} = \boldsymbol{u}^{(j,k)} + \epsilon_j\boldsymbol{r}$ with ϵ_j the expansion parameter and add the space independent constant $\boldsymbol{\Delta\Omega}^{(j,k)}$ to the stacking configuration of each layer. These refinements yield the following expressions for the stacking configurations of all interfaces:

$$\boldsymbol{\Omega}^{(1,k_1)}(\boldsymbol{U}) = -\frac{2\pi}{\alpha_2}(1+\delta)\,(A_1)^{-1}\Big(\boldsymbol{u}^{(1,k_1+1)} - \boldsymbol{u}^{(1,k_1)}\Big) + \boldsymbol{\Delta\Omega}^{(1,k_1+1)} - \boldsymbol{\Delta\Omega}^{(1,k_1)}, \tag{10a}$$

$$\boldsymbol{\Omega}^{(2,k_2)}(\boldsymbol{U}) = -\frac{2\pi}{\alpha_2}(A_1)^{-1}(A_{1\to2})^{-1}\Big(\boldsymbol{u}^{(2,k_2+1)} - \boldsymbol{u}^{(2,k_2)}\Big) + \boldsymbol{\Delta\Omega}^{(2,k_2+1)} - \boldsymbol{\Delta\Omega}^{(2,k_2)}, \tag{10b}$$

$$\boldsymbol{\Omega}^{(1\to2)}(\boldsymbol{U}) = \frac{2\pi}{\alpha_2}(A_1)^{-1}\Big(\big((1-\epsilon_2)(A_{1\to2})^{-1} - (1-\epsilon_1)(1+\delta)\mathbb{1}\big)\boldsymbol{r} - (A_{1\to2})^{-1}\boldsymbol{u}^{(2,1)} + (1+\delta)\boldsymbol{u}^{(1,n_1)}\Big) + \boldsymbol{\Delta\Omega}^{(2,1)} - \boldsymbol{\Delta\Omega}^{(1,n_1)}. \tag{10c}$$

In general, we formulate the stacking energy density of the system as a function of the relative stacking configurations $\boldsymbol{\Omega}$:

$$\mathcal{E}_{\text{stacking}}(\boldsymbol{U}) = \sum_{k_1=1}^{n_1-1} V_{\text{GSFE}}^{(1)}\big(\boldsymbol{\Omega}^{(1,k_1)}(\boldsymbol{U})\big) + \sum_{k_2=1}^{n_2-1} V_{\text{GSFE}}^{(2)}\big(\boldsymbol{\Omega}^{(2,k_2)}(\boldsymbol{U})\big) + V_{\text{GSFE}}^{(1\to2)}\big(\boldsymbol{\Omega}^{(1\to2)}(\boldsymbol{U})\big). \tag{11}$$

For the specific physical systems under consideration in this work, we we can use the known form of the GSFE functional [67–70] for each of the interfaces:

$$\begin{aligned} V_{\text{GSFE}}\Big(\boldsymbol{\Omega}, c_{0,\dots,5}\Big) &= c_0 \\ &+ c_1\big(\cos v + \cos w + \cos(v+w)\big) \\ &+ c_2\big(\cos(v+2w) + \cos(v-w) + \cos(2v+w)\big) \\ &+ c_3\big(\cos(2v) + \cos(2w) + \cos(2v+2w)\big) \\ &+ c_4\big(\sin v + \sin w - \sin(v+w)\big) \\ &+ c_5\big(\sin(2v+2w) - \sin(2v) - \sin(2w)\big), \end{aligned} \tag{12}$$

where we set $(v, w) = \boldsymbol{\Omega}$ as the components of the relative stacking configurations. The parameters $c_{0,\dots,5}$ depend on the type of interface. We therefore need three sets of parameters to calculate the stacking energy density, namely $c^{(j)}_{0,\dots,5}$ for each of the interfaces *within* flakes $j = 1, 2$ and $c^{(1\to2)}_{0,\dots,5}$ for the interface *between* flakes 1 and 2 (see Table II for numerical values for the systems under consideration in this work).

To find the solution $\boldsymbol{u}^{(j,k)}(\boldsymbol{r})$ and ϵ_j, we minimize the total energy

$$E_{\text{tot}} = \int \mathrm{d}^2 r \left(\mathcal{E}_{\text{stacking}}(\boldsymbol{U}) + \mathcal{E}_{\text{elastic}}(\nabla \boldsymbol{U}) \right) \tag{13}$$

using standard unconstrained minimization techniques (trust region algorithm). Note that changes to ϵ_j affect the size of the moiré unit cell, so one has to properly account for this effect in defining the grid and the strain terms.

III. MISMATCHED SYSTEM TEST CASE

Motivated by the experimental findings summarized in Fig. 2**(g,h)** we consider a $PdTe_2/Bi_2Se_3$ heterostructure as a specific example of a mismatched heterostructure. As the underlying Bravais lattice of both materials is triangular, the transformation matrix is trivial, i.e. $A_{1\to2} = \mathbb{1}$, and we set the lattice vectors as

$$\boldsymbol{a}_1 = \begin{pmatrix} 1 \\ 0 \end{pmatrix}, \qquad \boldsymbol{a}_2 = \begin{pmatrix} 1/2 \\ \sqrt{3}/2 \end{pmatrix}. \tag{14}$$

The GSFE function parameters $c_{1,\dots,5}$ for each interface of this multi-layered $PdTe_2$ on a Bi_2Se_3 substrate, and the bulk and shear moduli for both materials are taken from DFT (see Appendix C). For simplicity we fix the substrate and allow all $PdTe_2$ layers to relax individually. We further let the $PdTe_2$ flake expand isotropically via ϵ_2. This degree of freedom is crucial in order to explain the observation of Fig. 2**(g,h)**. Figure 3 summarizes the multi-layered relaxation results for different numbers of $PdTe_2$ layers. Figure 3**(a,b)** show how as the layer number drops the relaxation becomes stronger, leading to hexagonal domains and domain expansion. The domain expansion is further quantified in Fig. 3**(c)** covering the transition between the thick and thin $PdTe_2$ regimes. It is important to note that all the considered cases have shown a moiré period λ in excess of the accessible moiré periods as expected without including the isotropic expansion term (blue shaded region in Fig. 3**(c)**). Such an excess moiré period is in agreement with the experimental results. Our results highlight the multi-layered trade-off in search of an energy minimizing solution by the $PdTe_2$ flake: By conforming to the lattice constant of the Bi_2Se_3 substrate the stacking energy is reduced, at the expense of a penalty of an elastic energy. As the number of layers increases the elastic energy term becomes too costly and the relaxation is suppressed. However, at the thin $PdTe_2$ limit due to the relative softness

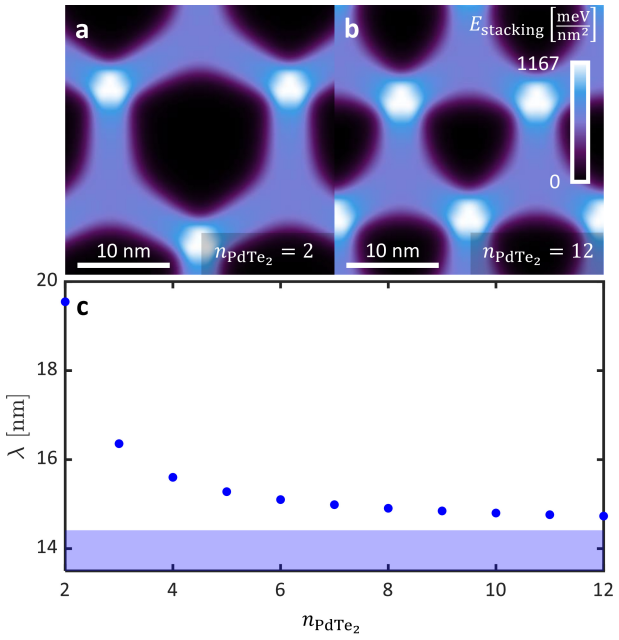

FIG. 3. **Modeling of thickness dependent moiré superlattice in $PdTe_2/Bi_2Se_3$.** **(a-b)** Moiré superlattice after mechanical relaxation visualized by the stacking energy density for 2 **(a)** and 12 **(b)** $PdTe_2$ layers on bulk Bi_2Se_3. **(c)** Moiré periodicity λ as a function of number of $PdTe_2$ layers. The blue region marks the range of accessible moiré period values without isotropic global strain. The relaxation calculations reveal enhanced relaxation and expansion of the moiré periodicity in the thin $PdTe_2$ layer limit. All considered cases assumed no twist between the $PdTe_2$ and the Bi_2Se_3. See calculation details in Appendix C.

of $PdTe_2$ (see Table II) the elastic energy penalty due to stretching the $PdTe_2$ is not severe in comparison with the stacking energy benefit, and the result is an enhanced moiré period. Figure 3**(c)** also highlights the penetration of the relaxation field (here probed by the layer dependent moiré periodicity λ) induced by the $PdTe_2/Bi_2Se_3$ interface into the stack which decays exponentially with the number of layers n_{PdTe_2}. To visualize the layer dependent moiré period, we assembled a video of the pattern in Fig. 3**(a,b)** varying n_{PdTe_2} over time [71].

IV. STRUCTURAL STUDY OF A GRAPHENE BASED SYSTEM

Next, we highlight the impact of employing the multi-layered relaxation scheme by the analysis of a graphene based system compared to the experimental findings reported in Fig. 2**(a-f)**. To this end, we study the structural properties of two flakes of Bernal stacked multi-layered graphene stacked with a twist at the interface of the two flakes. As in the previous section, the Bravais lattice of graphene is also triangular. However, we need to implement the twist angle θ as a two-dimensional ro-

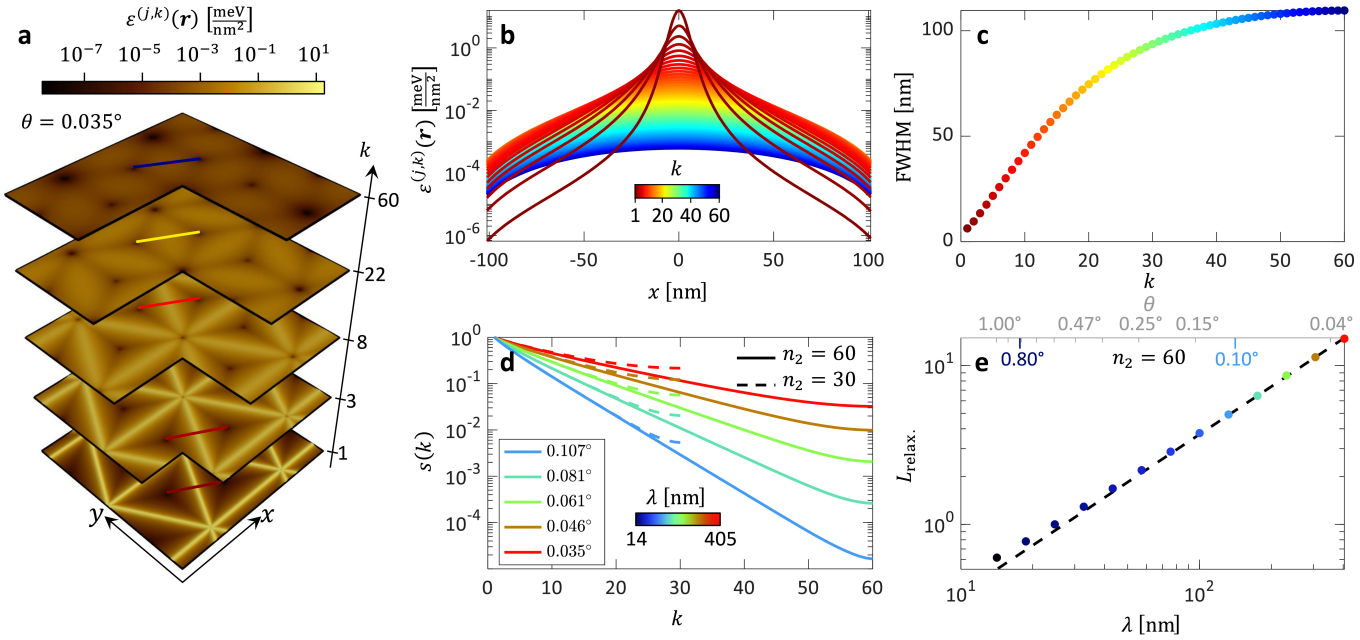

FIG. 4. **Multi-layered relaxation in twisted graphite interfaces (a)** Elastic energy density in representative layers for a $n_1 = n_2 = 60$ graphite on graphite structure with a twist angle $\theta = 0.035°$. **(b)** Domain wall (DW) profiles and **(c)** width as full width at half maximum (FWHM) for different layers showing the broadening and weakening of the relaxation away from the interface. Layer number indicated by color-bar in **(b)**. **(d)** Decay of the strength of the relaxation process away from the interface for different twist angles as captured by the displacement field scaling factor (see text for details). Two layer thickness cases are considered. **(e)** The penetration depth extracted from **(d)** as a function of the moiré period λ. The penetration depth is shown to be proportional to the moiré period (dashed line).

tation matrix in the transformation from flake 1 to 2: $A_{1\to 2} = R(\theta)$. Moreover, the GSFE parameters and shear and bulk moduli of graphene are presented in Appendix C.

As a primary result, we obtain the layer- and space-resolved elastic energy density $\varepsilon^{(j,k)}(\boldsymbol{r})$. This can be viewed as a layer-resolved elastic energy tomograph scanning through the height of the stacks. Figure 4**(a)** displays this result for a small twist angle system ($\theta = 0.035°$) and $n_1 = n_2 = 60$. The layer-resolved elastic energy tomograph emphasizes two main points: First, the relaxation pattern decays exponentially as a function of distance to the interface. Second, the system forms triangular relaxation domains separated by domain walls connecting the AB/BA regions of the interfacial moiré pattern. In Fig. 4**(b)**, we plot the elastic energy density along the line cut across a domain wall (as indicated in the tomograph of Fig. 4**(a)**) for all layers. At the interface, these domains have very sharp domain walls. The width of the domain wall grows as the distance to the interface increases, while at the same time its height declines. In Fig. 4**(c)** we quantify this behaviour by plotting the full width at half maximum (FWHM) as a function of layer index k. We color-code the value of k consistently across panels **(a-c)**.

Upon varying twist angle, we can examine how the relaxation behaviour evolves. To this end, we analyze the scaling of the atomic displacements $\boldsymbol{u}^{(j,k)}(\boldsymbol{r})$ as a function of k in the second flake $j = 2$. To do so we quantify the strength of the relaxation in layer k of flake 2 by defining a layer-dependent scaling factor $s(k)$ which is chosen such that the in-plane integrated squared difference

$$D(k) = \int \mathrm{d}^2 r \, \left\| \boldsymbol{u}^{(2,1)}(\boldsymbol{r}) - s(k)\boldsymbol{u}^{(2,k)}(\boldsymbol{r}) \right\|^2, \qquad (15)$$

of displacement fields of the k-th layer $\boldsymbol{u}^{(2,k)}(\boldsymbol{r})$ and the first layer $\boldsymbol{u}^{(2,1)}(\boldsymbol{r})$ is minimal.

Figure 4**(d)** shows the scaling factor $s(k)$ for five twist angles $0.035° \leq \theta \leq 0.107°$, with red curves corresponding to the small twist angle (large moiré wavelength λ) case and blue curves to the large twist angle (small λ) case. For each of the twist angles considered, we additionally set the number of layers of the second flake to $n_2 = 30$ (dashed lines) and $n_2 = 60$ (solid lines). Upto a cutoff when approaching the upper end of the stack (dependent on the height n_2), we find penetration of the relaxation fields into the stack which decays exponentially. The exponent decreases with the twist angle, yielding longer-ranged relaxation effects for smaller twist angle. We quantify the exponential decay of the relaxation effects by determining the penetration depth $L_{\text{relax.}}$ of the relaxation pattern. Here, we define $L_{\text{relax.}}$ through

$$s(k) \approx e^{-k/L_{\text{relax.}}} \qquad (16)$$

and calculate it using a fit for the case $n_2 = 60$ as a function of λ. The result is shown in Fig. 4**(e)** with consistent color-coding of λ and θ across panels **(d-e)**. We observe that the penetration depth $L_{\text{relax.}}(\lambda)$ scales linearly with λ in the small-θ and large-n_2 limit.

V. MULTI-LAYERED RELAXATION'S IMPACT ON THE ELECTRONIC STRUCTURE OF A GRAPHITIC SYSTEM

As suggested by our experimental data and confirmed by using the multi-layered relaxation framework, the in-plane relaxation can affect layers far from the interface of the flakes. For twisted graphitic systems this becomes particularly prominent at small twist angle (cf. Figs. 2 and 4). Such in-plane relaxations generate effective magnetic fields [72–75] and therefore may have a substantial impact on the electronic structure. Furthermore, using relaxed atomic positions has been shown to be crucial to explain low-energy properties of twisted graphitic systems [57–59, 76, 77]. Therefore, we analyze the effect of multi-layered relaxation on the electronic structure of twisted many-layer graphene systems in the following.

We focus on the case of several layers of Bernal stacked graphene on bulk graphite (corresponding to the small angle experimental PFM data shown in Fig. 2). We approximate the bulk by $n_1 = 20$ graphene layers and vary the number of layers in the top (twisted) flake from $n_2 = 3$ to $n_2 = 20$. We set the twist angle to $\theta = 0.1°$ (the $\theta = 0.8°$ case can be found in Appendix E) which implies a unit cell of ∼150 nm in size and ∼650,000 carbon atoms per layer. For a multi-layer geometry, the number of atoms is intractable for a tight-binding framework, and so we adopt the Bistritzer-MacDonald continuum model of twisted bilayer graphene [78–82] to include arbitrary in-plane relaxations (see Refs. 83 and 84) and Bernal multilayer hopping terms [63, 85–87].

For our analysis, we choose the twist angle θ to be commensurate. This implies a moiré unit cell with lattice vectors $\boldsymbol{L}_1 = \alpha\big(m\boldsymbol{a}_1 + n\boldsymbol{a}_2\big)$, $\boldsymbol{L}_2 = R(\pi/3)\boldsymbol{L}_1$, where (m, n) are integers and α the lattice constant of graphene. The Bistritzer-MacDonald Hamiltonian can be viewed as a reciprocal moiré lattice vector expansion of the full tight-binding Hamiltonian of the system. With $\boldsymbol{B}_{1,2}$ the reciprocal moiré lattice vectors, we therefore expect the multi-layered Hamiltonian to be a matrix in the "indices" $\boldsymbol{G} = p\boldsymbol{B}_1 + q\boldsymbol{B}_2$, $p, q \in \mathbb{N}$. The expansion is then truncated at $\|\boldsymbol{G}\| < G_c$, where G_c must be chosen large enough to ensure convergence. We further need to account for the sublattice (A, B), flake, layer, and valley $\xi = \pm 1$ degrees of freedom. For the sake of clarity of notation we drop flake indices and continuously index the layers with $l = 1, \ldots, n_1 + n_2$, where $l \leq n_1$ corresponds to flake $j = 1$ and $l > n_1$ to flake $j = 2$.

Our starting point is the intralayer continuum Hamiltonian, which is composed of the following three parts:

$$H_{\text{intra}}^{\boldsymbol{G}\boldsymbol{G}',\xi,l}(\boldsymbol{k}) = H_{\text{bernal}}^{\boldsymbol{G},\xi,l}(\boldsymbol{k})\delta_{\boldsymbol{G},\boldsymbol{G}'} + H_{\text{mag}}^{\boldsymbol{G}\boldsymbol{G}',\xi,l} + H_{\text{stat}}^{\boldsymbol{G}\boldsymbol{G}',\xi,l}. \tag{17}$$

Only the standard Bernal intralayer Hamiltonian explicitly depends on momentum $\boldsymbol{k}$ (in the moiré Brillouin zone). As the low-energy states all are close to the individual graphene layers' K_ξ-points, we shift and rotate the momentum vector:

$$\boldsymbol{K}_v = R(\theta^l)\left(\boldsymbol{k} - \boldsymbol{K}_\xi^l + \boldsymbol{G}\right), \tag{18}$$

with $R(\theta^{l>n_1}) = R(\theta)$ for the twisted layers in flake 2 and $R(\theta^{l\leq n_1}) = \mathbb{1}$ for the non-twisted layers in flake 1. The K_ξ-points of a given layer can be expressed by the reciprocal moiré lattice vectors as

$$\boldsymbol{K}_\xi^{l\leq n_1} = -\xi/3\left(2\boldsymbol{B}_2 + \boldsymbol{B}_1\right), \tag{19}$$

$$\boldsymbol{K}_\xi^{l>n_1} = -\xi/3\left(\boldsymbol{B}_2 - \boldsymbol{B}_1\right). \tag{20}$$

Using $K_v = \xi\boldsymbol{K}_{v,x} + i\boldsymbol{K}_{v,y}$, the Bernal intralayer Hamiltonian as a matrix in (A, B) sublattice space is then expressed as

$$H_{\text{bernal}}^{\boldsymbol{G},\xi,l}(\boldsymbol{k}) = \begin{pmatrix} \delta_{p,\text{A}} + \delta_{\text{isp}}^l & -v_F\, K_v^* \\ -v_F\, K_v & \delta_{p,\text{B}} + \delta_{\text{isp}}^l \end{pmatrix}. \tag{21}$$

Here, v_F denotes the Fermi velocity of graphene. We further include the intrinsic symmetric polarization δ_{isp}^l that is nonzero only in the central (twisted) layers: $\delta_{\text{isp}}^{n_1} = \delta_{\text{isp}}^{n_1+1} = \delta_{\text{isp}}$. Additionally, we account for sublattice polarization with $\delta_{p,\text{A}} = \delta_p$, $\delta_{p,\text{B}} = 0$ in all layers.

The other two parts of the intralayer continuum Hamiltonian Eq. (17) depend on the in-plane displacement field. As the in-plane displacement field is periodic in moiré lattice vectors and varies within the moiré unit cell, we apply a Fourier transform and obtain a representation in reciprocal moiré lattice vector space:

$$\boldsymbol{u}_{\boldsymbol{G}}^l = \sum_{\boldsymbol{r}} e^{-i\boldsymbol{G}\cdot\boldsymbol{r}}\boldsymbol{u}^{l=(j,k)}(\boldsymbol{r}). \tag{22}$$

First, we can write down the vector potential of the effective magnetic field generated by the displacement field as a function of $\boldsymbol{G}$:

$$\boldsymbol{A}^{\boldsymbol{G},l} = \begin{pmatrix} iG_x & -iG_y \\ -iG_y & -iG_x \end{pmatrix} \cdot \boldsymbol{u}_{\boldsymbol{G}}^l. \tag{23}$$

This potential is added to the Hamiltonian with a coupling strength g_2 by standard substitution:

$$H_{\text{mag}}^{\boldsymbol{G}\boldsymbol{G}',\xi,l} = g_2\left[\sigma_x A_x^{\boldsymbol{G}-\boldsymbol{G}',l} + \xi\sigma_y A_y^{\boldsymbol{G}-\boldsymbol{G}',l}\right], \tag{24}$$

with σ_x and σ_y Pauli matrices in sublattice space. Note that the initial dependency of the displacement field on the position vector $\boldsymbol{r}$ is translated to a (reciprocal moiré lattice) momentum transfer $\boldsymbol{G} - \boldsymbol{G}'$.

Second, the displacement field also generates a static potential that leads to the following contribution to the intralayer Hamiltonian:

$$H_{\text{stat}}^{\boldsymbol{GG}',\xi,l} = i\mathbb{1} g_1 \left[(\boldsymbol{G}-\boldsymbol{G}')\cdot \boldsymbol{u}^l_{\boldsymbol{G}-\boldsymbol{G}'}\right]. \tag{25}$$

Here, g_1 is the static potential's coupling strength.

The intralayer Hamiltonian is accompanied by several interlayer coupling terms. For all non-twisted interfaces, we employ an effective graphite Hamiltonian. Its coupling from one to the next layer reads (as a matrix in $(\mathrm{A}_l\mathrm{B}_l;\, \mathrm{A}_{l+1}\mathrm{B}_{l+1})$ sublattice space) [63, 87]

$$H_{\text{inter}}^{\boldsymbol{GG}',\xi,l\,l+1}(\boldsymbol{k}) = \begin{pmatrix} \gamma_4 K_v^* & \gamma_1 \\ \gamma_3 K_v^* & \gamma_4 K_v \end{pmatrix} \delta_{\boldsymbol{G},\boldsymbol{G}'}. \tag{26}$$

The coupling to second-next layers is taken into account as shown in Ref. 85 and reads as a matrix in $(\mathrm{A}_l\mathrm{B}_l;\, \mathrm{A}_{l+2}\mathrm{B}_{l+2})$:

$$H_{\text{inter}}^{\boldsymbol{GG}',\xi,l\,l+2}(\boldsymbol{k}) = \begin{pmatrix} \gamma_5 & 0 \\ 0 & \gamma_2 \end{pmatrix} \delta_{\boldsymbol{G},\boldsymbol{G}'}. \tag{27}$$

For the values of the hopping parameters $\gamma_{1,\dots,5}$ see Table I.

The interlayer Hamiltonian of the twisted interface between layers $l = n_1$ and $l = n_1 + 1$ encodes the interfacial moiré pattern and is therefore a matrix in $\boldsymbol{G}$. The coupling function U^ξ depends on the *difference* of in-plane displacement and is most easily formulated in real-space:

$$U^\xi(\boldsymbol{r}) = -\sum_{j=1}^{3} M_j^\xi\, t_0\, \exp\left[i\boldsymbol{Q}_j^\xi \cdot \left(\boldsymbol{u}^{(1,n_1)}(\boldsymbol{r}) - \boldsymbol{u}^{(2,1)}(\boldsymbol{r})\right) + i\delta\boldsymbol{k}_j\cdot\boldsymbol{r}\right]. \tag{28}$$

Here, t_0 is the out-of plane hopping and M_j^ξ are matrices in sublattice $(\mathrm{A}_{n_1},\mathrm{B}_{n_1};\, \mathrm{A}_{n_1+1},\mathrm{B}_{n_1+1})$ space:

$$M_1^\xi = \begin{pmatrix} 1 & c \\ c & 1 \end{pmatrix},\; M_2^\xi = \begin{pmatrix} 1 & c\,w^{-\xi} \\ c\,w^{\xi} & 1 \end{pmatrix},\; M_3^\xi = \left(M_2^\xi\right)^*, \tag{29}$$

with $c = 1.22333$ the ratio of AB-stacking to AA-stacking interlayer tunneling due to out-of plane corrugations and $w = \exp(2\pi i/3)$. The unperturbed momentum transfer vectors $\delta\boldsymbol{k}_j$ read

$$\delta\boldsymbol{k}_1 = 0\,,\quad \delta\boldsymbol{k}_2 = \xi\boldsymbol{B}_1\,,\quad \delta\boldsymbol{k}_3 = \xi(\boldsymbol{B}_1+\boldsymbol{B}_2)\,, \tag{30}$$

and the displacement induced momentum transfer vectors $\boldsymbol{Q}_j^\xi$ are the center of the twisted and non-twisted K_ξ-points of the original graphene lattices:

$$\boldsymbol{Q}_j^\xi = R(2\pi/3\,j)\left[\boldsymbol{K}_\xi^0 + \tilde{\boldsymbol{K}}_\xi^0\right]/2\,, \tag{31}$$

$$\boldsymbol{K}_{+1}^0 = -1/3\left(2\boldsymbol{b}_1+\boldsymbol{b}_2\right),\quad \boldsymbol{K}_{-1}^0 = R(2\pi/6)\boldsymbol{K}_{+1}^0\,, \tag{32}$$

$$\tilde{\boldsymbol{K}}_{+1}^0 = -1/3\left(2\tilde{\boldsymbol{b}}_1+\tilde{\boldsymbol{b}}_2\right),\quad \tilde{\boldsymbol{K}}_{-1}^0 = R(2\pi/6)\tilde{\boldsymbol{K}}_{+1}^0\,, \tag{33}$$

TABLE I. Parameters for setup of multi-layered continuum Hamiltonian. The length of the graphene lattice vectors $\boldsymbol{a}_{1,2}$ and the lattice constant α is needed for proper normalization of several hopping parameters.

$a = \alpha\lvert\lvert\boldsymbol{a}_1\rvert\rvert = \alpha\lvert\lvert\boldsymbol{a}_2\rvert\rvert$	$t_0 = 0.0797\,\text{eV}$
$\gamma_1 = 0.3513\,\text{eV}$	$\gamma_2 = -0.0105\,\text{eV}$
$\gamma_3 = 0.2973\,\text{eV}\cdot a\cdot\sqrt{3}/2$	$\gamma_4 = 0.1954\,\text{eV}\cdot a\cdot\sqrt{3}/2$
$\gamma_5 = 0.0187\,\text{eV}$	$\delta_p = 0.0540\,\text{eV}$
$\delta_{\text{isp}} = -0.03\,\text{eV}$	$g_2 = -6.3585\,\text{eV}$
$g_1 = 4.0\,\text{eV}$	$v_F = 2.1354\,\text{eV}\cdot a$

where $\boldsymbol{b}_{1,2}$ ($\tilde{\boldsymbol{b}}_{1,2}$) denote the reciprocal lattice vectors of the non-twisted (twisted) graphene lattice. To arrive at a consistent description we further take the Fourier transform of the real-space interlayer tunneling $U^\xi(\boldsymbol{r})$ and obtain a coupling function $U^{\boldsymbol{GG}',\xi}$.

The full single-particle continuum Hamiltonian for valley ξ follows as

$$H_\xi^{\boldsymbol{GG}',ll'}(\boldsymbol{k}) = H_{\text{intra}}^{\boldsymbol{GG}',\xi,l}(\boldsymbol{k})\,\delta_{l,l'} + H_{\text{inter}}^{\boldsymbol{GG}',\xi,ll'}(\boldsymbol{k})\,\delta_{\text{bulk}}^{ll'} + U^{\boldsymbol{GG}'}\,\delta_{\text{twist}}^{ll'}\,, \tag{34}$$

where $\delta_{\text{bulk}}^{ll'} = 1$ for l and l' in the same flake and $\delta_{\text{twist}}^{ll'} = 1$ for l and l' corresponding to the twisted interface coupling ($l = n_1$ to $l' = n_1+1$). For all other combinations of layers, these "delta functions" are zero. As the full Hamiltonian requires several numerical parameters, we provide an overview of their values in Table I.

The application of the continuum description Eq. (34) to the $\theta = 0.1°$ twisted many-layer graphene on graphite system is presented in the following. We inspect the local spectral density in the top layer of the twisted flake as an observable experimentally accessible by scanning tunneling microscopy. To isolate the effect of the relaxation we compare the rigid system (where $\boldsymbol{u}^{(j,k)}(\boldsymbol{r}) \equiv 0$) to the relaxed one where we apply the method of Section II to find $\boldsymbol{u}^{(j,k)}(\boldsymbol{r})$.

The left subpanels in Fig. 5 present the integrated (over space) top layer density of states (DOS) as a function of energy ω. Over all panels **(a-f)**, the top flake layer number n_2 is varied from $n_2 = 8$ to $n_2 = 20$ (the $n_2 = 3$ to $n_2 = 6$ cases are shown in Appendix E). We subdivide the rigid **(a,c,e)** and the relaxed **(b,d,f)** cases. To highlight the spatial variations, we color the curves with the coefficient of variation of the top layer LDOS (over space) that is defined as

$$c_{\text{v}}(l,\omega) = \frac{\text{std}_{\boldsymbol{r}}\left(\text{LDOS}(l,\omega,\boldsymbol{r})\right)}{\text{mean}_{\boldsymbol{r}}\left(\text{LDOS}(l,\omega,\boldsymbol{r})\right)}\,. \tag{35}$$

Additionally, we add a gray background that corresponds to the minimum/maximum values taken by the LDOS of

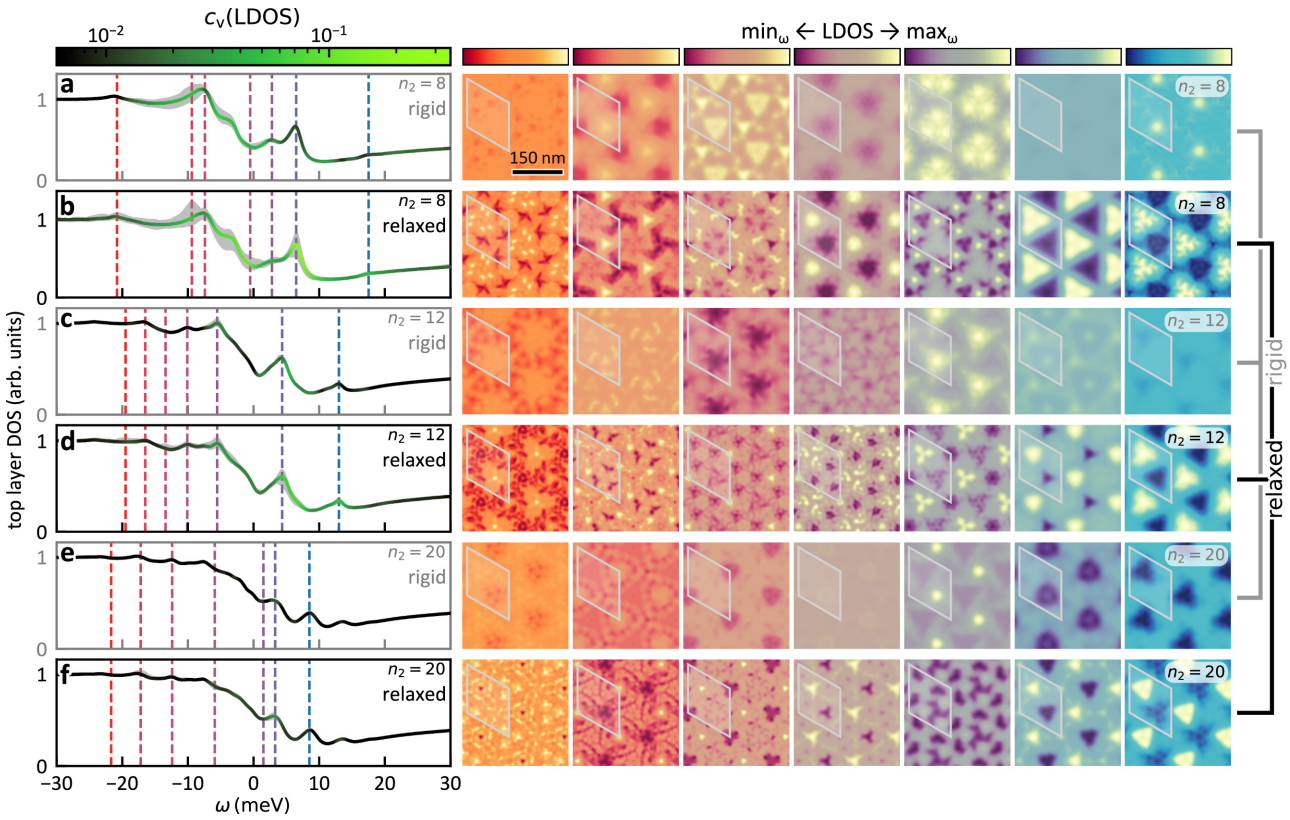

FIG. 5. **Electronic structure properties for graphite on graphite at twist angle of $\theta = 0.1°$.** Each row **(a-f)** corresponds to the same system where we vary the number of graphene layers in the top flake (n_2) and relaxed/rigid atomic structures across rows. Left subpanels: Frequency (ω) resolved density of states (DOS) of the outermost layer of the top graphite flake. Panels **(a,c,e)** represent simulations using rigid structures and panels **(b,d,f)** relaxed structures. The number of layers of the bottom flake is fixed at $n_1 = 20$. We color-code the coefficient of variation ($c_v = \sigma/\mu$) of the local density of states (LDOS) in the top layer as a function of ω. Light green indicates strong spatial variations in the top layer LDOS, whereas black corresponds to a uniform LDOS. The gray area in the background of the curves indicates the minimum and maximum values of the LDOS. Right subpanels: Spatial distribution of the LDOS in the outermost layer at a given frequency. The frequencies are indicated in the left subpanels as dashed, colored vertical lines varying from red (low frequencies) to blue (high frequencies). The color-maps for the LDOS maps are chosen to be consistent with this coloring. Light (yellow) regions correspond to high intensity and dark (red $\rightarrow$ blue) regions to low intensity. For each configuration, the rigid (gray) and relaxed (black) panels in two subsequent rows share a color scale to make differences visible. The system's unit cell is indicated in each of the small subpanels. All plots on the right hand side share the scale bar plotted in the top left subpanel.

the outermost layer. By the DOS and its spatial variations we can identify regions in ω (for each n_2) where the effect of relaxation is most pronounced. We highlight these regions by vertical dashed lines colored from red to blue. The right subpanels in each row **(a-f)** show the corresponding spatial map of the outermost layer LDOS for these specific ω and n_2 values. Note that two subsequent rows [e.g. **(a)** and **(b)**] share a color-map for each ω and n_2 such that differences from the relaxed to the rigid case become visible. The color-maps of the LDOS maps are chosen to correspond to the colors indicating ω in the DOS plot on the left. We provide the LDOS maps for all frequencies as videos in the supplemental material [71]. For $n_2 = 8$ and $n_2 = 12$, the LDOS maps for rigid atomic structures **(a,c)** clearly show less variation than the ones for relaxed atomic structures **(b,d)** for all values of ω chosen. Likewise, the c_v value is much larger over a substantial range of frequencies [see left subpanels for **(a-d)**]. The local density of states shows strong differences between the rigid and relaxed calculations in these cases. At a twist angle of $\theta = 0.1°$ this highlights the relevance of relaxation effects for a description of the electronic properties. At $n_2 = 20$, over a broad range of frequencies the value of c_v is minor in both the relaxed **(f)** and rigid **(e)** case. Only at around $\omega \approx 3\,\text{meV}$ there is a slightly more pronounced spatial variation showing that for the twist angle of $\theta = 0.1°$ the effects of relaxation do not penetrate through $n_2 = 20$ layers in accord with the analysis of $s(k)$ above suggesting $L_{\text{relax.}} \sim 5$ layers.

VI. OUTLOOK

Our work highlights the effects of multi-layered relaxation in various vdW heterostructures. We have shown experimentally using PFM that for multi-layered graphene stacks with a twisted interface the atomic displacement can propagate deep into the flake for small twist angles [see Fig. 2 **(a-f)**]. We complement this experimental observation of the relevance of relaxation in twisted vdW heterostructures with an untwisted mismatched system: multi-layered $PdTe_2$ on a Bi_2Se_3 substrate. In this system, multi-layered relaxation is of great importance as well and it becomes distinctively visible as a change in lattice constant as the number of $PdTe_2$ layers is increased [cf. Fig. 2 **(g,h)**]. We thus establish that multi-layered relaxation is highly relevant for the engineering of stacked vdW heterostructures in the twisted and non-twisted context. On the one hand this emphasizes the need of deepened understanding of relaxation and a refinement of the lego-like picture often employed in the field [1]. On the other hand, it adds yet another tuning knob to the thriving field of vdW heterostructure engineering. As exemplified here for $PdTe_2$ on a Bi_2Se_3 substrate, the effective lattice constant can be tuned over a rather versatile range by multi-layered relaxation effects.

In tandem, we develop a machinery that allows us to simulate and understand these relaxation properties given the generalized stacking fault energy functional from *ab-initio* calculations. Within this approach, we treat each layer of the heterostructure stack as a separate membrane. Our simulations fully support the experimental evidence of three dimensional, layered relaxation patterns in both systems: First, we reproduce the stacking height dependent lattice constant evolution in a stack of $PdTe_2$ on Bi_2Se_3 (Fig. 3). Second, we observe that the penetration depth of relaxation domains in twisted graphite stacks linearly increases with moiré wavelength (Fig. 4). These two examples emphasize how the three dimensional nature of multi-layered heterostructures needs to be taken into account when modeling their atomic structure.

Ultimately we predict differences in electronic properties arising from the atomic relaxation in multi-layered graphene twisted on graphite. Similarly to the notion of penetration depth of the relaxation pattern, we see that the local density of states in the outermost layer of the graphene stack sensitively depends on whether the atomic positions of the crystal are relaxed or not. For a small twist angle ($\theta = 0.1°$), we demonstrate that the local variation of the electron density in the outermost graphene layer is much stronger when the multi-layered relaxation pattern is taken into account properly (Fig. 5). We propose to analyze such multi-layered (small angle) twisted graphene on graphite stacks using scanning tunneling microscopy in the future, as the local electronic density as a function of frequency can be used to probe the here predicted effects of relaxation on the electronic structure in precise manner. The strong effects of relaxation on the electronic properties of the stack highlight that also these properties, including their collective behavior, can be engineered by the relaxation of stacked vdW heterostructure even beyond the few layer paradigm.

ACKNOWLEDGMENTS

Nano-imaging research at Columbia is supported by DOE-BES grant DE-SC0018426. Research on atomic relaxation is supported by W911NF2120147. We acknowledge funding by the Deutsche Forschungsgemeinschaft (DFG, German Research Foundation) under RTG 1995 and RTG 2247, within the Priority Program SPP 2244 "2DMP", under Germany's Excellence Strategy - Cluster of Excellence Matter and Light for Quantum Computing (ML4Q) EXC 2004/1 - 390534769 and - Cluster of Excellence and Advanced Imaging of Matter (AIM) EXC 2056 - 390715994. We acknowledge computational resources provided by the Max Planck Computing and Data Facility and RWTH Aachen University under project number rwth0716. This work was supported by the Max Planck-New York City Center for Nonequilibrium Quantum Phenomena. DNB is Moore Investigator in Quantum Materials EPIQS GBMF9455. DH was supported by a grant from the Simons Foundation (579913).

Appendix A: Graphene experiment

Using an optical microscope, we identify exfoliated graphene flakes with tiered graphene thicknesses in close proximity to a bulk graphite flake from the same crystal. Samples are then assembled using a dry transfer technique using a slide with polycarbonate (PC) film on top of a polydimethyl siloxane (PDMS) dome [88]. We use the slide to first pick up a BN flake of thickness $30 - 40\,\text{nm}$, which is then placed into contact with the bulk graphite flake. After picking up the bulk graphite, we then rotationally misalign the transfer stage by a small angle of less than 1 degree before picking up the tiered graphene flake. The completed heterostructure remains on the polymer stamp slide during subsequent experimental measurements.

We use piezoresponse force microscopy (PFM) to image the moiré superlattice between the rotationally misaligned tiered graphene flake and the bulk graphite [89]. In PFM, we apply an AC bias between the conductive probe and the microscope stage, which induces a periodic deformation of the sample through the piezoelectric effect. The phase and amplitude of the local deformation provide the strongest contrast to visualize moiré in our samples. AC bias magnitudes were $500 - 1000\,\text{mV}$ with resonance frequencies in the range of $270 - 300\,\text{kHz}$ for vertical and $750 - 850\,\text{kHz}$ for lateral PFM. The experiments were performed in a Bruker Dimension Icon with a

Nanoscope V Controller, using Oxford Instrument Asylum Research ASYELEC-01 Ti/Ir coated silicon probes.

Appendix B: $PdTe_2/Bi_2Se_3$ experiment

The $PdTe_2$ thin films were grown on a Bi_2Se_3 substrate in an integrated MBE-STM ultrahigh vacuum (UHV) system with base pressure below 2×10^{-10} mbar. The Bi_2Se_3 was prepared by in-situ cleaving the surface and subsequent annealing to 250 °C for one hour to degas. Then, high-purity Pd (99.95%) and Te (99.9999%) were evaporated from an electron-beam evaporator and a standard Knudsen cell, respectively, with a flux ratio of 1:10. The deposition rate of Pd and Te atoms was monitored by a quartz oscillator. The temperature of substrate was kept at 210 °C during the growth.

After the initial annealing of the Bi_2Se_3, the substrate was transferred in-situ to the Aarhus STM stage with a Tungsten tip. STM measurements were taken of the substrate to ensure the quality of the substrate. Once deposition of the Pd and Te was complete, the sample was transferred in-situ to the STM stage for surface topography mapping.

Appendix C: Material parameters used for the relaxation calculations

The material parameters used for the multilayer graphene relaxations, consisting of the GSFE coefficients $c_{0,\dots,5}$ and strain (bulk and shear) moduli K and G, are taken from Ref. 67. For the $PdTe_2/Bi_2Se_3$ multilayer simulations, the three interfacial GSFE functionals, strain moduli, and monolayer lattice parameters were extracted from density functional calculations performed with the Vienna Ab initio Simulation Package (VASP) [90]. A monolayer geometry was used to calculate the α, K, and G values for both materials, and a two-layer geometry was used for the three different GSFEs ($PdTe_2/PdTe_2$, $PdTe_2/Bi_2Se_3$, and Bi_2Se_3/Bi_2Se_3). The numerical values of all material parameters relevant for relaxing the atomic structures are given in Table II. In all cases, the out-of-plane c axis (parallel to z) was set to 30 Å to ensure no interaction between the periodic slabs. The van der Waals energy functional SCAN+rVV10 [91] was used alongside PAW-PBE pseudo potentials for all atoms [92]. A plane wave energy cutoff of 300 eV and electronic convergence of 10^{-5} eV were used, with dipole corrections turned on for the out-of-plane (c, or z) axis. Optimization of the lattice constant for the monolayer, and out-of-plane relaxation of the atoms for the interfacial calculations, were performed via conjugate gradient descent with a 10^{-4} eV convergence criterion.

TABLE II. Material parameters for the $PdTe_2/Bi_2Se_3$ and graphene based heterostructures used for the relaxation calculations in this work. $c_{0,\dots,5}$ are the GSFE coefficients of Eq. (12) for the $PdTe_2/PdTe_2$, Bi_2Se_3/Bi_2Se_3, $PdTe_2/Bi_2Se_3$ and the graphene/graphene interfaces (u.c. stands for the area of the 2D unit cell). α are the lattice constants for $PdTe_2$, Bi_2Se_3 and graphene. K and G stand for the bulk and shear moduli.

	$PdTe_2$	Bi_2Se_3	$PdTe_2/Bi_2Se_3$	Graphene
$c_0\,[\frac{\text{meV}}{\text{u.c.}}]$	157.73	59.19	102.65	6.832
$c_1\,[\frac{\text{meV}}{\text{u.c.}}]$	-41.10	22.80	28.21	4.064
$c_2\,[\frac{\text{meV}}{\text{u.c.}}]$	-6.25	-4.76	-6.47	-0.374
$c_3\,[\frac{\text{meV}}{\text{u.c.}}]$	-5.23	-0.21	-1.66	-0.095
$c_4\,[\frac{\text{meV}}{\text{u.c.}}]$	5.63	1.71	11.17	0
$c_5\,[\frac{\text{meV}}{\text{u.c.}}]$	1.18	2.53	5.54	0
α [Å]	4.014	4.129	–	2.47
$K\,[\frac{\text{meV}}{\text{u.c.}}]$	30902	47049	–	69518
$G\,[\frac{\text{meV}}{\text{u.c.}}]$	17759	25995	–	47352

Appendix D: LDOS from continuum model

Spectral densities generally can be defined in an arbitrary basis of the Hamiltonian. The layer-resolved local density of states, i.e. LDOS$(l, \omega, \boldsymbol{r})$, is nothing else but the spectral density in a basis consisting of real-space-, layer-, sublattice-, valley- and momentum-indices. The sublattice (x), valley and momentum degrees of freedom are summed over to obtain a function of l and $\boldsymbol{r}$, and frequency ω. As our model Eq. (34) is forumlated in reciprocal moiré lattice vector ($\boldsymbol{G}$) space, we obtain the following Green's function:

$$G^{\boldsymbol{G}\boldsymbol{G}',\xi,ll',xx'}(i\omega,\boldsymbol{k}) = \sum_b \frac{u^b_{\boldsymbol{G},\xi,l,x}(\boldsymbol{k})\left[u^b_{\boldsymbol{G}',\xi,l',x'}(\boldsymbol{k})\right]^*}{i\omega - \epsilon^b_\xi(\boldsymbol{k})}\,, \tag{D1}$$

with b a band index and $\epsilon^b_\xi(\boldsymbol{k})$ the dispersion of band b of valley ξ at momentum $\boldsymbol{k}$. Note that, since the Hamiltonian is diagonal in the valleys $\xi = \pm 1$, the Green's function carries only one valley index as well. For a real-space description, we need to transform the $\boldsymbol{G}$ indices to real-space:

$$G^{\boldsymbol{r}\boldsymbol{r}',\xi,ll',xx'}(i\omega,\boldsymbol{k}) = \frac{1}{N_{\boldsymbol{G}}}\sum_{\boldsymbol{G}\boldsymbol{G}'} e^{-i(\boldsymbol{G}\cdot\boldsymbol{r}-\boldsymbol{G}'\cdot\boldsymbol{r}')} \times G^{\boldsymbol{G}\boldsymbol{G}',\xi,ll',xx'}(i\omega,\boldsymbol{k})\,. \tag{D2}$$

Here, the number of reciprocal moiré lattice vectors $N_{\boldsymbol{G}}$ is needed for proper normalization. The representation in a diagonal basis, Eq. (D1), numerically facilitates the Fourier transform: Instead of transforming both indices

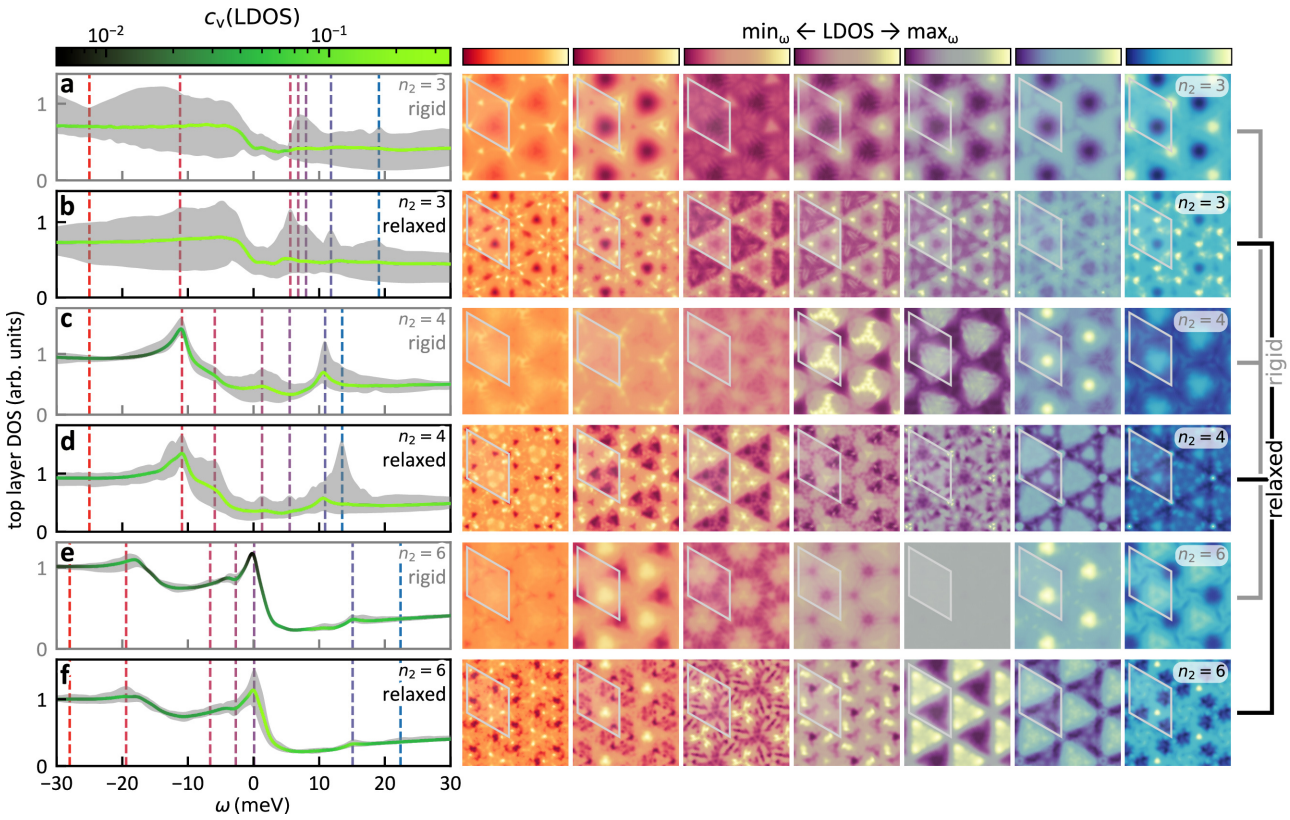

FIG. 6. **Small angle ($\theta = 0.1°$) electronic structure of few-layer graphene on graphite.** The number of layers of the first graphite flake is set to $n_1 = 20$, whereas the number of layers of the second graphite flake is varied from $n_2 = 3$ **(a,b)** over $n_2 = 4$ **(c,d)** to $n_2 = 6$ **(e,f)**. In panels (rows) **(a,c,e)** we used rigid atomic positions and in **(b,d,f)** relaxed ones. The color of the lines in the left subpanels codes the coefficient of variation of the top layer LDOS, with green as non-uniform regions and black as uniform regions. The gray background is given by the minimum/maximum values of the LDOS. On the right, we show LDOS maps at selected frequencies indicated in the left subpanels. Each subsequent two rows [e.g. **(a)** and **(b)**] share a color-map for each frequency such that differences in relaxed and rigid structures are apparent.

in a double sum [cf. Eq. (D2)], we can directly transform the "Bloch"-functions $u^b_{\boldsymbol{G},\xi,l,x}(\boldsymbol{k})$ to real-space:

$$u^b_{\boldsymbol{r},\xi,l,x}(\boldsymbol{k}) = \frac{1}{\sqrt{N_{\boldsymbol{G}}}} \sum_{\boldsymbol{G}} e^{-i\boldsymbol{G}\cdot\boldsymbol{r}}\, u^b_{\boldsymbol{G},\xi,l,x}(\boldsymbol{k})\,. \tag{D3}$$

Then we perform the analytic continuation $i\omega \to \omega + i\eta$ and trace out the sublattice-, valley- and momentum-indices to arrive at

$$\mathrm{LDOS}(l,\omega,\boldsymbol{r}) = -\mathrm{Im} \sum_{\xi,x,\boldsymbol{k},b} \frac{|u^b_{\boldsymbol{r},\xi,l,x}(\boldsymbol{k})|^2}{\epsilon^b_\xi(\boldsymbol{k}) - \omega + i\eta}\,. \tag{D4}$$

The broadening parameter η determines the energy resolution. We set $\eta = 5\,\mathrm{meV}$ for all simulations of the $\theta = 0.8°$ systems and $\eta = 0.8\,\mathrm{meV}$ for the $\theta = 0.1°$ case. The momentum summation is carried out on an equispaced mesh with 14×14 points in a C_3 reduced wedge of the Brillouin zone.

For numerical calculations of the system's electronic properties we employ specialized code operating on a hybrid CPU/multi-GPU (OpenMP/CUDA) architecture. Convergence of the inverse moiré lattice vector expansion dictates large matrix sizes for the Hamiltonian. The expansion's cutoff G_c is set by magnitude: $\|\boldsymbol{G}\| < G_c$. In the case of $\theta = 0.1°$ we require $G_c = 13\|\boldsymbol{B}_{1/2}\|$ for convergence resulting in Hamilton matrix sizes of ∼50,000 (for $n_1 = n_2 = 20$). In the large angle case ($\theta = 0.8°$) we set $G_c = 5\|\boldsymbol{B}_{1/2}\|$ to converge the expansion.

Appendix E: Additional Electronic Structure Data

1. Small angle case with few-layered graphene

We here present the additional cases of $n_2 = 3$, $n_2 = 4$, and $n_2 = 6$ for the small angle ($\theta = 0.1°$) system with $n_1 = 20$. Figure 6 displays the results in the same manner as Fig. 5 in the main text.

The six panels **(a-f)** correspond to the LDOS data of rigid/relaxed systems at $n_2 = 3$, $n_2 = 4$, and $n_2 = 6$. The left subpanel shows the spatially integrated LDOS of the outermost layer with color coding as the coefficient of variation (over space). Here, black corresponds to small

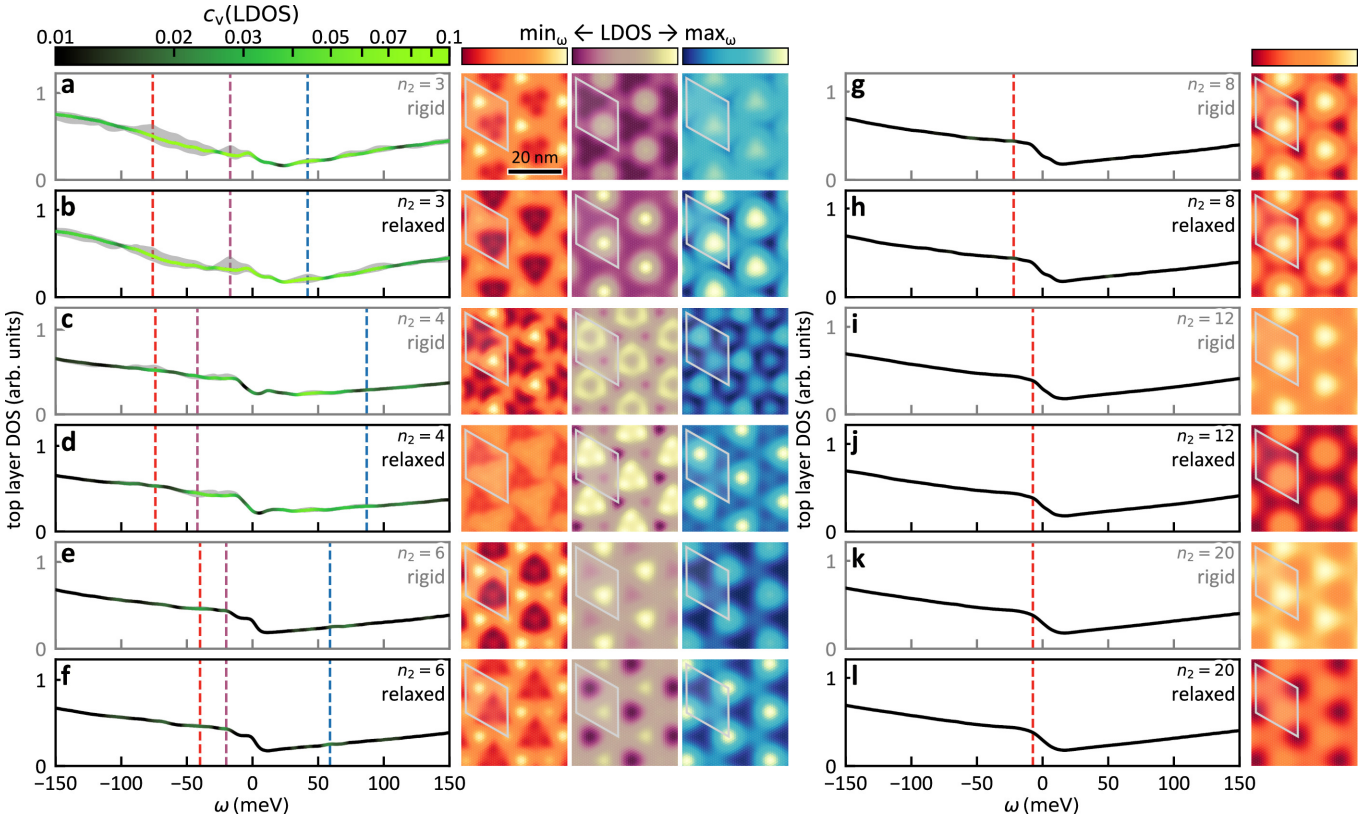

FIG. 7. **Overview over electronic structure of many-layer graphene twisted at $\theta = 0.8°$ on graphite system** Similarly to Figs. 5 and 6, we display the integrated top layer DOS and additionally color-code the coefficient of variation c_v. Furthermore, we mark the minimum/maximum values taken by the top layer LDOS as gray background. The system considered here also consists of $n_1 = 20$ layers of graphene as a bottom flake and $n_2 = 3, \ldots, 20$ layers of graphene as a top flake. In Panels **(a-f)**, we vary n_2 from 3 over 4 to 6, with subsequent rows corresponding to the relaxed and rigid cases of the same system. The subpanels on the right show the LDOS maps at selected frequencies indicated as vertical dashed lines in the left subpanels. The color-maps correspond to the vertical dashed lines' colors. Two subsequent rows [e.g. **(a)** and **(b)**] share a color-map for each frequency to make differences apparent. **(g-l)** Same as panels **(a-f)**, but for $n_2 = 8$, $n_2 = 12$, and $n_2 = 20$. As for these systems local variations in the electronic density of the top layer are very minuscule, we only show the LDOS maps at a single frequency. Apart from a small shift in absolute scale, these LDOS maps are very similar between each relaxed and rigid case in panels **(g-l)**.

variation, i.e. a uniform LDOS and green corresponds to large variation, i.e. a spatially non-uniform LDOS. Additionally, we add the minimum/maximum values taken by the top layer LDOS as gray background. At selected frequencies, we show the explicit spacial distribution of the LDOS for each system on the right hand side in the same row. The color-maps of the LDOS maps are normalized for the rigid and relaxed cases of a single n_2, i.e. subsequent rows [e.g. panels **(a)** and **(b)**] share a color-map normalization. The color-scheme of the LDOS maps evolves as a function of frequency to match the color of the vertical dashed lines indicating the exact frequency values. Even in the few-layer (small angle) data in Fig. 6, we observe the tendency that, when increasing n_2, the local variations in top layer LDOS are strongly enhanced for the relaxed case.

2. Large angle case

To highlight the importance of small twist angles for large penetration depths of relaxation effects into the stack, we here present the analysis of the electronic structure for a twist angle of $\theta = 0.8°$. As in Section V and Appendix E 1, the number of graphene layers in the bottom flake is fixed at $n_1 = 20$ and we vary the number of graphene layers in the top flake from $n_2 = 3$ to $n_2 = 20$. The results are presented in Figure 7. Overall, we observe that patterns in the LDOS of the top layer decay much faster as a function of increasing n_2. For example, even the $n_2 = 6$ and $n_2 = 8$ cases display no notable difference in c_v of the relaxed and rigid structures. For $n_2 \geq 8$, the value of c_v is too small to be visible on the selected scale (less than 1%). Furthermore, no such clear pattern of increased c_v in the relaxed case over the rigid case can be found as for the small angle ($\theta = 0.1°$) case.

We interpret this behaviour as the relaxation decaying as fast – or faster than – the effects that the moiré interlayer coupling $U^{\boldsymbol{G},\boldsymbol{G}'}$ has on the top layer electronic structure.

3. Full frequency LDOS maps

As supplemental material [71], we provide all LDOS maps for the systems studied within this work as videos where we change ω with each frame. The color-maps evolve as a function of ω similar to the color-maps of the LDOS maps in Figs. 5, 6 and 7. The upper panel corresponds to the rigid structure and the lower panel to the relaxed one. In each frame, we normalize the color-map separately with bright (yellow) colors indicating maxima and dark (red/blue) colors indicating minima. To display only significant LDOS variations in the movies, we set the minimum relative difference that needs to be covered by the color-map to $\pm 2\%$ such that when the minimum and maximum values are closer than 2% to their mean value, we artificially increase the color-mapped minimum and maximum values to be 2% away from the mean value.

[1] A. K. Geim and I. V. Grigorieva, Van der waals heterostructures, Nature **499**, 419 (2013).

[2] M. Wang, S. K. Jang, W.-J. Jang, M. Kim, S.-Y. Park, S.-W. Kim, S.-J. Kahng, J.-Y. Choi, R. S. Ruoff, Y. J. Song, and S. Lee, A platform for large-scale graphene electronics – cvd growth of single-layer graphene on cvd-grown hexagonal boron nitride, Advanced Materials **25**, 2746 (2013).

[3] H. Wang, F. Liu, W. Fu, Z. Fang, W. Zhou, and Z. Liu, Two-dimensional heterostructures: fabrication, characterization, and application, Nanoscale **6**, 12250 (2014).

[4] T. Niu and A. Li, From two-dimensional materials to heterostructures, Progress in Surface Science **90**, 21 (2015).

[5] K. Novoselov, o. A. Mishchenko, o. A. Carvalho, and A. Castro Neto, 2d materials and van der waals heterostructures, Science **353**, aac9439 (2016).

[6] Y. Cao, V. Fatemi, S. Fang, K. Watanabe, T. Taniguchi, E. Kaxiras, and P. Jarillo-Herrero, Unconventional superconductivity in magic-angle graphene superlattices, Nature **556**, 43 (2018).

[7] X. Lu, P. Stepanov, W. Yang, M. Xie, M. A. Aamir, I. Das, C. Urgell, K. Watanabe, T. Taniguchi, G. Zhang, A. Bachtold, A. H. MacDonald, and D. K. Efetov, Superconductors, orbital magnets and correlated states in magic-angle bilayer graphene, Nature **574**, 653 (2019).

[8] M. Yankowitz, S. Chen, H. Polshyn, Y. Zhang, K. Watanabe, T. Taniguchi, D. Graf, A. F. Young, and C. R. Dean, Tuning superconductivity in twisted bilayer graphene, Science **363**, 1059 (2019).

[9] Y. Cao, D. Rodan-Legrain, J. M. Park, F. N. Yuan, K. Watanabe, T. Taniguchi, R. M. Fernandes, L. Fu, and P. Jarillo-Herrero, Nematicity and competing orders in superconducting magic-angle graphene, arXiv preprint arXiv:2004.04148 (2020).

[10] X. Liu, Z. Wang, K. Watanabe, T. Taniguchi, O. Vafek, and J. Li, Tuning electron correlation in magic-angle twisted bilayer graphene using coulomb screening, Science **371**, 1261 (2021).

[11] P. Stepanov, I. Das, X. Lu, A. Fahimniya, K. Watanabe, T. Taniguchi, F. H. Koppens, J. Lischner, L. Levitov, and D. K. Efetov, Untying the insulating and superconducting orders in magic-angle graphene, Nature **583**, 375 (2020).

[12] H. S. Arora, R. Polski, Y. Zhang, A. Thomson, Y. Choi, H. Kim, Z. Lin, I. Z. Wilson, X. Xu, J.-H. Chu, *et al.*, Superconductivity in metallic twisted bilayer graphene stabilized by wse 2, Nature **583**, 379 (2020).

[13] M. Oh, K. P. Nuckolls, D. Wong, R. L. Lee, X. Liu, K. Watanabe, T. Taniguchi, and A. Yazdani, Evidence for unconventional superconductivity in twisted bilayer graphene, Nature **600**, 240–245 (2021).

[14] J. M. Park, Y. Cao, K. Watanabe, T. Taniguchi, and P. Jarillo-Herrero, Tunable strongly coupled superconductivity in magic-angle twisted trilayer graphene, Nature **590**, 249 (2021).

[15] Y. Cao, J. M. Park, K. Watanabe, T. Taniguchi, and P. Jarillo-Herrero, Pauli-limit violation and re-entrant superconductivity in moiré graphene, Nature **595**, 526–531 (2021).

[16] Z. Hao, A. Zimmerman, P. Ledwith, E. Khalaf, D. H. Najafabadi, K. Watanabe, T. Taniguchi, A. Vishwanath, and P. Kim, Electric field–tunable superconductivity in alternating-twist magic-angle trilayer graphene, Science **371**, 1133 (2021).

[17] H. Kim, Y. Choi, C. Lewandowski, A. Thomson, Y. Zhang, R. Polski, K. Watanabe, T. Taniguchi, J. Alicea, and S. Nadj-Perge, Spectroscopic signatures of strong correlations and unconventional superconductivity in twisted trilayer graphene (2021), arXiv:2109.12127 [cond-mat.mes-hall].

[18] Y. Cao, V. Fatemi, A. Demir, S. Fang, S. L. Tomarken, J. Y. Luo, J. D. Sanchez-Yamagishi, K. Watanabe, T. Taniguchi, E. Kaxiras, R. C. Ashoori, and P. Jarillo-Herrero, Correlated insulator behaviour at half-filling in magic-angle graphene superlattices, Nature **556**, 80 (2018).

[19] Y. Cao, D. Chowdhury, D. Rodan-Legrain, O. Rubies-Bigordà, K. Watanabe, T. Taniguchi, T. Senthil, and P. Jarillo-Herrero, Strange metal in magic-angle graphene with near planckian dissipation, Phys. Rev. Lett. **124**, 076801 (2020).

[20] H. Polshyn, M. Yankowitz, S. Chen, Y. Zhang, K. Watanabe, T. Taniguchi, C. R. Dean, and A. F. Young, Large linear-in-temperature resistivity in twisted bilayer graphene, Nat. Phys. **15**, 1011 (2019).

[21] U. Zondiner, A. Rozen, D. Rodan-Legrain, Y. Cao, R. Queiroz, T. Taniguchi, K. Watanabe, Y. Oreg, F. von Oppen, A. Stern, E. Berg, P. Jarillo-Herrero, and S. Ilani, Cascade of phase transitions and dirac revivals in magic-angle graphene, Nature **582**, 203 (2020).

[22] D. Wong, K. P. Nuckolls, M. Oh, B. Lian, S. J. Yonglong Xie, K. Watanabe, T. Taniguchi, B. A.

Bernevig, and A. Yazdani, Cascade of electronic transitions in magic-angle twisted bilayer graphene, Nature **582**, 198–202 (2020).

[23] Y. Xie, B. Lian, B. Jäck, X. Liu, C.-L. Chiu, K. Watanabe, T. Taniguchi, B. A. Bernevig, and A. Yazdani, Spectroscopic signatures of many-body correlations in magic-angle twisted bilayer graphene, Nature **572**, 101 (2019).

[24] A. Kerelsky, L. J. McGilly, D. M. Kennes, L. Xian, M. Yankowitz, S. Chen, K. Watanabe, T. Taniguchi, J. Hone, C. Dean, A. Rubio, and A. N. Pasupathy, Maximized electron interactions at the magic angle in twisted bilayer graphene, Nature **572**, 95 (2019).

[25] Y. Jiang, X. Lai, K. Watanabe, T. Taniguchi, K. Haule, J. Mao, and E. Y. Andrei, Charge order and broken rotational symmetry in magic-angle twisted bilayer graphene, Nature **573**, 91 (2019).

[26] Y. Choi, J. Kemmer, Y. Peng, A. Thomson, H. Arora, R. Polski, Y. Zhang, H. Ren, J. Alicea, G. Refael, F. von Oppen, K. Watanabe, T. Taniguchi, and S. Nadj-Perge, Electronic correlations in twisted bilayer graphene near the magic angle, Nat. Phys. **15**, 1174 (2019).

[27] S. Chen, M. He, Y.-H. Zhang, V. Hsieh, Z. Fei, K. Watanabe, T. Taniguchi, D. H. Cobden, X. Xu, C. R. Dean, *et al.*, Electrically tunable correlated and topological states in twisted monolayer–bilayer graphene, Nature Physics **17**, 374 (2021).

[28] Y. Shi, S. Xu, M. M. A. Ezzi, N. Balakrishnan, A. Garcia-Ruiz, B. Tsim, C. Mullan, J. Barrier, N. Xin, B. A. Piot, *et al.*, Tunable van hove singularities and correlated states in twisted trilayer graphene, arXiv preprint arXiv:2004.12414 (2020).

[29] X. Liu, Z. Hao, E. Khalaf, J. Y. Lee, Y. Ronen, H. Yoo, D. Haei Najafabadi, K. Watanabe, T. Taniguchi, A. Vishwanath, *et al.*, Tunable spin-polarized correlated states in twisted double bilayer graphene, Nature **583**, 221 (2020).

[30] C. Shen, Y. Chu, Q. Wu, N. Li, S. Wang, Y. Zhao, J. Tang, J. Liu, J. Tian, K. Watanabe, *et al.*, Correlated states in twisted double bilayer graphene, Nature Physics **16**, 520 (2020).

[31] Y. Cao, D. Rodan-Legrain, O. Rubies-Bigorda, J. M. Park, K. Watanabe, T. Taniguchi, and P. Jarillo-Herrero, Tunable correlated states and spin-polarized phases in twisted bilayer–bilayer graphene, Nature **583**, 215 (2020).

[32] L. Wang, E.-M. Shih, A. Ghiotto, L. Xian, D. A. Rhodes, C. Tan, M. Claassen, D. M. Kennes, Y. Bai, B. Kim, *et al.*, Correlated electronic phases in twisted bilayer transition metal dichalcogenides, Nature materials **19**, 861 (2020).

[33] Y. Tang, L. Li, T. Li, Y. Xu, S. Liu, K. Barmak, K. Watanabe, T. Taniguchi, A. H. MacDonald, J. Shan, *et al.*, Simulation of hubbard model physics in wse2/ws2 moiré superlattices, Nature **579**, 353 (2020).

[34] E. C. Regan, D. Wang, C. Jin, M. I. Bakti Utama, B. Gao, X. Wei, S. Zhao, W. Zhao, Z. Zhang, K. Yumigeta, *et al.*, Mott and generalized wigner crystal states in wse2/ws2 moiré superlattices, Nature **579**, 359 (2020).

[35] P. K. Nayak, Y. Horbatenko, S. Ahn, G. Kim, J.-U. Lee, K. Y. Ma, A.-R. Jang, H. Lim, D. Kim, S. Ryu, *et al.*, Probing evolution of twist-angle-dependent interlayer excitons in mose2/wse2 van der waals heterostructures, ACS nano **11**, 4041 (2017).

[36] P. Rivera, H. Yu, K. L. Seyler, N. P. Wilson, W. Yao, and X. Xu, Interlayer valley excitons in heterobilayers of transition metal dichalcogenides, Nature nanotechnology **13**, 1004 (2018).

[37] E. M. Alexeev, D. A. Ruiz-Tijerina, M. Danovich, M. J. Hamer, D. J. Terry, P. K. Nayak, S. Ahn, S. Pak, J. Lee, J. I. Sohn, *et al.*, Resonantly hybridized excitons in moiré superlattices in van der waals heterostructures, Nature **567**, 81 (2019).

[38] T. I. Andersen, G. Scuri, A. Sushko, K. De Greve, J. Sung, Y. Zhou, D. S. Wild, R. J. Gelly, H. Heo, D. Bérubé, *et al.*, Excitons in a reconstructed moiré potential in twisted wse2/wse2 homobilayers, Nature Materials **20**, 480 (2021).

[39] C. Jin, E. C. Regan, A. Yan, M. Iqbal Bakti Utama, D. Wang, S. Zhao, Y. Qin, S. Yang, Z. Zheng, S. Shi, *et al.*, Observation of moiré excitons in wse2/ws2 heterostructure superlattices, Nature **567**, 76 (2019).

[40] G. W. Burg, J. Zhu, T. Taniguchi, K. Watanabe, A. H. MacDonald, and E. Tutuc, Correlated insulating states in twisted double bilayer graphene, Physical review letters **123**, 197702 (2019).

[41] C. Rubio-Verdú, S. Turkel, Y. Song, L. Klebl, R. Samajdar, M. S. Scheurer, J. W. Venderbos, K. Watanabe, T. Taniguchi, H. Ochoa, *et al.*, Moiré nematic phase in twisted double bilayer graphene, Nature Physics , 1 (2021).

[42] G. Chen, A. L. Sharpe, P. Gallagher, I. T. Rosen, E. J. Fox, L. Jiang, B. Lyu, H. Li, K. Watanabe, T. Taniguchi, *et al.*, Signatures of tunable superconductivity in a trilayer graphene moiré superlattice, Nature **572**, 215 (2019).

[43] G. Chen, L. Jiang, S. Wu, B. Lyu, H. Li, B. L. Chittari, K. Watanabe, T. Taniguchi, Z. Shi, J. Jung, *et al.*, Evidence of a gate-tunable mott insulator in a trilayer graphene moiré superlattice, Nature Physics **15**, 237 (2019).

[44] G. Chen, A. L. Sharpe, E. J. Fox, Y.-H. Zhang, S. Wang, L. Jiang, B. Lyu, H. Li, K. Watanabe, T. Taniguchi, *et al.*, Tunable correlated chern insulator and ferromagnetism in a moiré superlattice, Nature **579**, 56 (2020).

[45] K. P. Nuckolls, M. Oh, D. Wong, B. Lian, K. Watanabe, T. Taniguchi, B. A. Bernevig, and A. Yazdani, Strongly correlated chern insulators in magic-angle twisted bilayer graphene, Nature **588**, 610 (2020).

[46] Y. Xie, A. T. Pierce, J. M. Park, D. E. Parker, E. Khalaf, P. Ledwith, Y. Cao, S. H. Lee, S. Chen, P. R. Forrester, *et al.*, Fractional chern insulators in magic-angle twisted bilayer graphene, Nature **600**, 439 (2021).

[47] A. T. Pierce, Y. Xie, J. M. Park, E. Khalaf, S. H. Lee, Y. Cao, D. E. Parker, P. R. Forrester, S. Chen, K. Watanabe, *et al.*, Unconventional sequence of correlated chern insulators in magic-angle twisted bilayer graphene, Nature Physics **17**, 1210 (2021).

[48] P. Stepanov, M. Xie, T. Taniguchi, K. Watanabe, X. Lu, A. H. MacDonald, B. A. Bernevig, and D. K. Efetov, Competing zero-field chern insulators in superconducting twisted bilayer graphene, Physical review letters **127**, 197701 (2021).

[49] Y. Choi, H. Kim, Y. Peng, A. Thomson, C. Lewandowski, R. Polski, Y. Zhang, H. S. Arora, K. Watanabe, T. Taniguchi, *et al.*, Tracing out correlated chern insulators in magic angle twisted bilayer graphene, arXiv preprint arXiv:2008.11746 (2020).

[50] A. L. Sharpe, E. J. Fox, A. W. Barnard, J. Finney, K. Watanabe, T. Taniguchi, M. Kastner, and

D. Goldhaber-Gordon, Emergent ferromagnetism near three-quarters filling in twisted bilayer graphene, Science **365**, 605 (2019).

[51] S. Wu, Z. Zhang, K. Watanabe, T. Taniguchi, and E. Y. Andrei, Chern insulators, van hove singularities and topological flat bands in magic-angle twisted bilayer graphene, Nature materials **20**, 488 (2021).

[52] I. Das, X. Lu, J. Herzog-Arbeitman, Z.-D. Song, K. Watanabe, T. Taniguchi, B. A. Bernevig, and D. K. Efetov, Symmetry-broken chern insulators and rashba-like landau-level crossings in magic-angle bilayer graphene, Nature Physics **17**, 710 (2021).

[53] J. M. Park, Y. Cao, K. Watanabe, T. Taniguchi, and P. Jarillo-Herrero, Flavour hund's coupling, chern gaps and charge diffusivity in moiré graphene, Nature **592**, 43 (2021).

[54] Y. Saito, J. Ge, K. Watanabe, T. Taniguchi, and A. F. Young, Independent superconductors and correlated insulators in twisted bilayer graphene, Nature Physics **16**, 926 (2020).

[55] D. M. Kennes, M. Claassen, L. Xian, A. Georges, A. J. Millis, J. Hone, C. R. Dean, D. N. Basov, A. N. Pasupathy, and A. Rubio, Moiré heterostructures as a condensed-matter quantum simulator, Nature Physics **17**, 155 (2021).

[56] S. Carr, S. Fang, and E. Kaxiras, Electronic-structure methods for twisted moiré layers, Nature Reviews Materials **5**, 748–763 (2020).

[57] K. Uchida, S. Furuya, J.-I. Iwata, and A. Oshiyama, Atomic corrugation and electron localization due to moiré patterns in twisted bilayer graphenes, Phys. Rev. B **90**, 155451 (2014).

[58] P. Lucignano, D. Alfè, V. Cataudella, D. Ninno, and G. Cantele, Crucial role of atomic corrugation on the flat bands and energy gaps of twisted bilayer graphene at the magic angle $\theta \sim 1.08^\circ$, Phys. Rev. B **99**, 195419 (2019).

[59] F. Guinea and N. R. Walet, Continuum models for twisted bilayer graphene: the effects of lattice deformation and hopping parameters, Phys. Rev. B **99**, 205134 (2019).

[60] G. Cantele, D. Alfè, F. Conte, V. Cataudella, D. Ninno, and P. Lucignano, Structural relaxation and low energy properties of twisted bilayer graphene, arXiv:2004.14323v1 (2020).

[61] M. H. Naik and M. Jain, Ultraflatbands and Shear Solitons in Moiré Patterns of Twisted Bilayer Transition Metal Dichalcogenides, Physical Review Letters **121**, 266401 (2018).

[62] F. Gargiulo and O. V. Yazyev, Structural and electronic transformation in low-angle twisted bilayer graphene, 2D Materials **5**, 10.1088/2053-1583/aa9640 (2018).

[63] F. Haddadi, Q. S. Wu, A. J. Kruchkov, and O. V. Yazyev, Moiré Flat Bands in Twisted Double Bilayer Graphene, Nano Letters **20**, 2410 (2020).

[64] M. Van Wijk, A. Schuring, M. Katsnelson, and A. Fasolino, Relaxation of moiré patterns for slightly misaligned identical lattices: graphene on graphite, 2D Materials **2**, 034010 (2015).

[65] I. Maity, P. K. Maiti, H. R. Krishnamurthy, and M. Jain, Reconstruction of moiré lattices in twisted transition metal dichalcogenide bilayers, Physical Review B **103**, L121102 (2021).

[66] S. K. Jain, V. Juričić, and G. T. Barkema, Structure of twisted and buckled bilayer graphene, 2D Materials **4**, 015018 (2016).

[67] S. Carr, D. Massatt, S. B. Torrisi, P. Cazeaux, M. Luskin, and E. Kaxiras, Relaxation and domain formation in incommensurate two-dimensional heterostructures, Physical Review B **98**, 224102 (2018).

[68] Z. Zhu, S. Carr, D. Massatt, M. Luskin, and E. Kaxiras, Twisted Trilayer Graphene: A Precisely Tunable Platform for Correlated Electrons, Physical Review Letters **125**, 1 (2020).

[69] P. Cazeaux, M. Luskin, and D. Massatt, Energy Minimization of Two Dimensional Incommensurate Heterostructures, Archive for Rational Mechanics and Analysis **235**, 1289 (2020).

[70] D. Halbertal, N. R. Finney, S. S. Sunku, A. Kerelsky, C. Rubio-Verdú, S. Shabani, L. Xian, S. Carr, S. Chen, C. Zhang, L. Wang, D. Gonzalez-Acevedo, A. S. McLeod, D. Rhodes, K. Watanabe, T. Taniguchi, E. Kaxiras, C. R. Dean, J. C. Hone, A. N. Pasupathy, D. M. Kennes, A. Rubio, and D. N. Basov, Moiré metrology of energy landscapes in van der Waals heterostructures, Nature Communications **12**, 1 (2021).

[71] D. Halbertal, L. Klebl, V. Hsieh, J. Cook, S. Carr, G. Bian, C. Dean, D. M. Kennes, and D. N. Basov, Supplementary material (2022).

[72] S. V. Morozov, K. S. Novoselov, M. I. Katsnelson, F. Schedin, L. A. Ponomarenko, D. Jiang, and A. K. Geim, Strong suppression of weak localization in graphene, Phys. Rev. Lett. **97**, 016801 (2006).

[73] M. Vozmediano, M. Katsnelson, and F. Guinea, Gauge fields in graphene, Physics Reports **496**, 109 (2010).

[74] M. I. Katsnelson, *Graphene: Carbon in Two Dimensions* (Cambridge University Press, 2012).

[75] B. Amorim, A. Cortijo, F. de Juan, A. Grushin, F. Guinea, A. Gutiérrez-Rubio, H. Ochoa, V. Parente, R. Roldán, P. San-Jose, J. Schiefele, M. Sturla, and M. Vozmediano, Novel effects of strains in graphene and other two dimensional materials, Physics Reports **617**, 1 (2016), novel effects of strains in graphene and other two dimensional materials.

[76] N. N. Nam and M. Koshino, Lattice relaxation and energy band modulation in twisted bilayer graphene, Physical Review B **96**, 1 (2017).

[77] X. Liang, Z. A. H. Goodwin, V. Vitale, F. Corsetti, A. A. Mostofi, and J. Lischner, Effect of bilayer stacking on the atomic and electronic structure of twisted double bilayer graphene, Phys. Rev. B **102**, 155146 (2020).

[78] R. Bistritzer and A. H. MacDonald, Moiré bands in twisted double-layer graphene, Proceedings of the National Academy of Sciences **108**, 12233 (2011), https://www.pnas.org/content/108/30/12233.full.pdf.

[79] J. M. B. Lopes dos Santos, N. M. R. Peres, and A. H. Castro Neto, Continuum model of the twisted graphene bilayer, Phys. Rev. B **86**, 155449 (2012).

[80] J. M. B. Lopes dos Santos, N. M. R. Peres, and A. H. Castro Neto, Graphene bilayer with a twist: Electronic structure, Phys. Rev. Lett. **99**, 256802 (2007).

[81] M. Koshino, N. F. Q. Yuan, T. Koretsune, M. Ochi, K. Kuroki, and L. Fu, Maximally localized wannier orbitals and the extended hubbard model for twisted bilayer graphene, Phys. Rev. X **8**, 031087 (2018).

[82] T. Cea, N. R. Walet, and F. Guinea, Twists and the electronic structure of graphitic materials, Nano Letters **19**, 8683 (2019), pMID: 31743649, https://doi.org/10.1021/acs.nanolett.9b03335.

[83] L. Balents, General continuum model for twisted bilayer graphene and arbitrary smooth deformations, SciPost Phys. **7**, 48 (2019).

[84] M. Koshino and N. N. T. Nam, Effective continuum model for relaxed twisted bilayer graphene and moiré electron-phonon interaction, Phys. Rev. B **101**, 195425 (2020).

[85] A. Grüneis, C. Attaccalite, L. Wirtz, H. Shiozawa, R. Saito, T. Pichler, and A. Rubio, Tight-binding description of the quasiparticle dispersion of graphite and few-layer graphene, Phys. Rev. B **78**, 205425 (2008).

[86] M. Koshino, Band structure and topological properties of twisted double bilayer graphene, Phys. Rev. B **99**, 235406 (2019).

[87] R. Samajdar and M. S. Scheurer, Microscopic pairing mechanism, order parameter, and disorder sensitivity in moiré superlattices: Applications to twisted double-bilayer graphene, Phys. Rev. B **102**, 064501 (2020).

[88] L. Wang, I. Meric, P. Y. Huang, Q. Gao, Y. Gao, H. Tran, T. Taniguchi, K. Watanabe, L. M. Campos, D. A. Muller, J. Guo, P. Kim, J. Hone, Shepard, and C. R. Dean, One-Dimensional Electrical Contact to a Two-Dimensional Material, Science **342**, 614 (2013).

[89] L. J. McGilly, A. Kerelsky, N. R. Finney, K. Shapovalov, E. M. Shih, A. Ghiotto, Y. Zeng, S. L. Moore, W. Wu, Y. Bai, K. Watanabe, T. Taniguchi, M. Stengel, L. Zhou, J. Hone, X. Zhu, D. N. Basov, C. Dean, C. E. Dreyer, and A. N. Pasupathy, Visualization of moiré superlattices, Nature Nanotechnology **15**, 580 (2020).

[90] G. Kresse and J. Furthmüller, Efficient iterative schemes for ab initio total-energy calculations using a plane-wave basis set, Phys. Rev. B **54**, 11169 (1996).

[91] H. Peng, Z.-H. Yang, J. P. Perdew, and J. Sun, Versatile van der waals density functional based on a meta-generalized gradient approximation, Phys. Rev. X **6**, 041005 (2016).

[92] G. Kresse and D. Joubert, From ultrasoft pseudopotentials to the projector augmented-wave method, Phys. Rev. B **59**, 1758 (1999).